2019

Effect of Al alloying on cavitation erosion behavior of TaSi2 nanocrystalline coatings

Jiang Xu

Shuai Kang Zhang

Xiao Lin Lu

Shuyun Jiang

Paul Munroe

See next page for additional authors

10.1016/j.ultsonch.2019.104742

Xu, J., Zhang, S. K., Lu, X. L., Jiang, S., Munroe, P., & Xie, Z.-H. (2019). Effect of Al alloying on cavitation erosion behavior of TaSi2 nanocrystalline coatings. *Ultrasonics Sonochemistry*, *59*, Article 104742. Available here

Ultrasonics - Sonochemistry 59 (2019) 104742

Contents lists available at ScienceDirect

Ultrasonics - Sonochemistry

journal homepage: www.elsevier.com/locate/ultson

Effect of Al alloying on cavitation erosion behavior of $TaSi_2$ nanocrystalline coatings

Jiang Xu[a,*], Shuai Kang Zhang[a], Xiao Lin Lu[a], Shuyun Jiang[b], Paul Munroe[c], Zong-Han Xie[d,e]

[a] Department of Material Science and Engineering, Nanjing University of Aeronautics and Astronautics, 29 Yudao Street, Nanjing 210016, PR China
[b] Department of Mechanical Engineering, Southeast University, 2 Si Pai Lou, Nanjing 210096, PR China
[c] School of Materials Science and Engineering, University of New South Wales, NSW 2052, Australia
[d] School of Mechanical Engineering, University of Adelaide, SA 5005, Australia
[e] School of Engineering, Edith Cowan University, Perth, WA 6027, Australia

ARTICLE INFO

Keywords:
Refractory metal silicides
First-principle calculations
Cavitation erosion
Potentiodynamic polarization
EIS

ABSTRACT

To broaden the scope of non-aerospace applications for titanium-based alloys, both hexagonal C40 binary $TaSi_2$ and ternary Al alloyed $TaSi_2$ nanocrystalline coatings were exploited to enhance the cavitation erosion resistance of Ti-6Al-4V alloy in acidic environments. To begin with, the roles of Al addition in influencing the structural stability and mechanical properties of hexagonal C40 $Ta(Si_{1-x}Al_x)_2$ compounds were modelled using first-principles calculations. The calculated key parameters, such as Pugh's index (B/G ratio), Poisson's ratio, and Cauchy pressures, indicated that there was a threshold value for Al addition, below which the increase of Al content would render the $Ta(Si_{1-x}Al_x)_2$ compounds more ductile, but above which no obvious change would occur. Subsequently, the $TaSi_2$ and $Ta(Si_{0.875}Al_{0.125})_2$ coatings were prepared and their microstructure and phase composition were characterized by X-ray diffraction (XRD), scanning electron microscopy (SEM) and transmission electron microscopy (TEM). Both the two coatings exhibited a uniform thickness of 15 μm and a densely packed structure mainly composed of spherically shaped nanocrystallites with an average diameter of about 5 nm. Nanoindentation measurements revealed that Al alloying reduced the hardness (H) and elastic modulus (E) values of the $TaSi_2$ coating. Ultrasonic cavitation erosion tests were carried out by immersing coated and uncoated samples in a 0.5 M HCl solution. The cavitation-erosion analysis of the tested samples was investigated by various electrochemical techniques, mass loss weight and SEM observation. The results suggested that both coated samples provided a better protection for Ti-6Al-4V against the cavitation-erosion damage in acidic environments, but the addition of Al further improved the cavitation-erosion resistance of the $TaSi_2$ coating.

1. Introduction

Through their unique combination of high strength-to-weight ratio and excellent resistance to corrosion, titanium alloys are increasingly finding new industrial application outside military and commercial aerospace fields, for example in the petrochemical and chemical industries [1]. The low dissolution rate of titanium alloys under most corrosive media is due to the presence of stable, continuous and protective passive films that form on the alloy surface. Despite its high corrosion resistance in various media, the naturally formed passive film lacks sufficient mechanical stability and is readily removed in some harsh environments, especially where the occurrence of corrosion is directly related to mechanical degradation processes (e.g. erosion, cavitation, abrasion, etc.). Therefore, much attention has been paid to improving the resistance of titanium alloys against a combined erosion-corrosion attack.

Cavitation erosion is the most common type of material degradation in overflow components in hydrodynamic systems, for example marine propellers or hydraulic pumps or turbines [2]. The formation of cavities stems from the tensile stress imposed on the liquid as the local pressure drops below the vapor pressure of the fluid produced by flow fluctuation (vibration) or motion of the solid boundary [3]. When these cavities migrate to higher pressure zones, they collapse violently, exerting pressure shock waves and liquid micro-jets on to adjacent solid surfaces. The combined action of pressure pulses and fatigue processes incurred from the repetitive shock waves and micro jets causes severe cavitation damage of flow-handling components and leads to premature failure [4]. If the cavitating liquid is an aggressive aqueous solution, cavitation erosion and corrosion can take place simultaneously. The corrosion-enhanced cavitation-erosion aggravates the removal of the protective oxide film on the solid surface, since the mass loss can increase significantly beyond that due to either cavitation-erosion or

* Corresponding author.
E-mail address: xujiang73@nuaa.edu.cn (J. Xu).

https://doi.org/10.1016/j.ultsonch.2019.104742
Received 19 March 2019; Received in revised form 20 August 2019; Accepted 21 August 2019
Available online 22 August 2019

corrosion alone [5]. The resistance to cavitation erosion for titanium alloys depends largely on their microstructure and mechanical properties, as well as the cavitation medium etc. Hou et al. [6] found that the microstructure of Ti-6Al-4V plays a significant part in its cavitation erosion behavior in deionized water. When Ti-6Al-4V was exposed to cavitation, induced by the repeated bubble collapse, the bcc structured β-phase was more readily removed with respect to the hcp structured α-phase. This resulted in fatigue fracture of the remnant protuberant α-lathes and led to signnificant cavitation erosion damage. Mochizuki et al. [7] investigated the cavitation erosion behavior of various titanium alloys using a rotating disk method in seawater. They showed that the cavitation erosion resistance was proportional to the Vickers hardness of the tested samples. Further, Li et al. [8] studied the effects of SiO_2 particles on ultrasonic cavitation erosion of Ti-6Al-4V in a 0.1 M H_2SO_4 solution. It was shown that the mean depth of erosion of the alloy sharply decreased with increasing particle concentration and size.

For either corrosion or cavitation erosion in corrosive liquids, material degradation primarily occurs at the liquid/solid interface, that is dependent on surface, rather than bulk properties. Recently, much research has focused on improvement in the surface properties of titanium alloys under cavitation, through exploitation of surface engineering techniques. Mann et al. [9] reported that a laser-treated twin wire arc-sprayed SHS 7170 coating significantly improved the cavitation erosion resistance of Ti-6Al-4V. Further, Man et al. [10] examined the cavitation erosion behavior of laser gas nitrided commercial titanium alloys in a 3.5% NaCl solution. Their results showed that the cavitation erosion resistance was improved by an order of magnitude through surface treatment. Higher cavitation erosion resistance of the nitrided layer was attributed to an increase in surface hardness as well as the fine, dendritic microstructure of the TiN layer. Amongst the various surface modification technologies currently available, the double cathode glow discharge deposition method has been proven to be an effective approach to improve the wear resistance, corrosion resistance and oxidation resistance of titanium alloys through the deposition of nanocrystalline silicides coatings [11].

Transition metal silicides (TMS) possess unique combinations of outstanding physical and chemical properties, such as excellent resistance to high temperature oxidation, low density, high melting points and creep strength, endowing them with potential as candidate materials for high temperature applications [12]. Among these silicides, $TaSi_2$, that exhibits a hexagonal structure with a $P6_222$ space group, has found wide applications in the semiconductor industry, because of its superconductivity and good contact ability with silicon. In particular, $TaSi_2$ shows great potential for use as a wear-corrosion resistant material, due to its high hardness and good corrosion resistance. However, similar to other metal disilicides, its poor room temperature toughness inhibits its widespread application. Usually, alloying with certain alloy elements to replace metal and Si sites in disilicides has been shown a fruitful path to increase toughness [12]. Our recent work has shown that the Al alloyed β-Ta_5Si_3 has a higher resistance to erosion-corrosion and ultrasonic cavitation erosion as compared to the binary β-Ta_5Si_3 coating and 316L stainless steel[13].

In this work, the influence of Al additions on the structural stability and elastic properties of $TaSi_2$ were systematically studied using first-principle calculations, in order to improve the understanding of the Al alloying on the brittle-or-ductile behavior of $TaSi_2$ at an atomic level. These theoretical results are valuable for the optimization of Al content in this compound. As a consequence, the binary $TaSi_2$ and ternary Ta$(Si_{0.875}Al_{0.125})_2$ coatings were deposited onto Ti-6Al-4V substrates using the double cathode glow discharge technique. The mechanical behavior and cavitation erosion behavior in a 0.5 M HCl solution for the two coatings were investigated and compared to the bare substrate.

2. Theoretical and experimental methods

2.1. Computational method

In this work, all the first-principles calculations for binary $TaSi_2$ and ternary Al alloyed $TaSi_2$ were conducted by using the density functional theory (DFT), as implemented in the Cambridge serial total energy package (CASTEP) code [14]. To compare the calculated results, the exchange correlation functional was treated by the generalized gradient approximation (GGA) with the Perdew-Burke-Ernzerhof (PBE) functional [15]. Ultrasoft pseudopotentials were used to describe the interactions between the ion core and valance electrons. The electronic configurations for the pseudo-atoms were Ta $5d^36s^2$, Si $3s^23p^2$ and Al $3s^23p^1$, respectively. As seen from Fig. 1, a 2 × 2 × 1 supercell consisting of 12 Ta atoms and 24 Si atoms was constructed for the binary C40-structured $TaSi_2$ and a series of ternary C40-structured Ta$(Si_{1-x}Al_x)_2$ supercells were built by replacing Si atoms by 1, 2, 3 and 4 Al atoms, where the corresponding Al concentrations (i.e., the value of subscript *x*) were 0.042, 0.083, 0.125 and 0.167, respectively. Based on the convergence testing for the total energy at ground state, a plane-wave cutoff energy of 400 eV for both the binary and ternary Ta$(Si_{1-x}Al_x)_2$ were deemed adequate to achieve good convergence. According to the Monkhorst-Pack scheme, Brillouin zone integration was performed with a 4 × 4 × 4 k-point mesh for the Ta$(Si_{1-x}Al_x)_2$ supercell model. The tolerances of the geometrical optimization met the following conditions: total energy changes less than 2×10^{-6} eV/atom, maximum ionic Hellmann-Feynman force below 0.01 eV/Å, maximum stress lower than 0.02 GPa and maximum ionic displacement within 2×10^{-4} Å. The elastic constants (C_{ij}) for Ta$(Si_{1-x}Al_x)_2$ were determined from evaluation of stress tensor generated small strains [16]. According to the calculated C_{ij} values, mechanical properties such as bulk modulus (B), Young's modulus (E), shear modulus (G) and Poisson's ratio (υ) could be derived using the Voigt-Reuss-Hill approximations method [17].

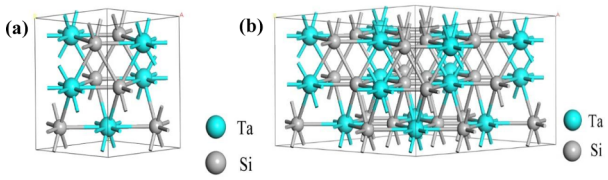

Fig. 1. The optimized structures of (a) the primitive cell for $TaSi_2$ and (b) the 2 × 2 × 1 supercells for $TaSi_2$.

2.2. Specimen preparation

Ti-6Al-4V discs (Ø40 mm × 3 mm), with the nominal composition in wt%: Al, 6.04; V, 4.03; Fe, 0.3; O, 0.1; C, 0.1; N, 0.05; H, 0.015 and the balance, Ti, were used as substrates. Prior to deposition, the substrate samples were ground with different grades of silicon carbide papers and finally polished using 0.05 μm diamond pastes. Subsequently, the polished substrate samples were ultrasonically cleaned in ethanol and finally dried in cold air. A double cathode glow discharge system (Wuhan Shoufar Surface Engineering Ltd.) was employed to prepare both the binary and ternary Ta$(Si_{1-x}Al_x)_2$ coatings using two targets with different stoichiometric ratios ($Ta_{20}Si_{80}$ and $Ta_{20}Si_{70}Al_{10}$), respectively. The chamber was evacuated to a base pressure of 5×10^{-4} Pa. To remove any contamination from the surface of the substrates prior to deposition, the samples were cleaned by Ar ion bombardment at a potential of −650 V for 20 min. During sputter deposition, the pressure in the chamber was maintained at 35 Pa with an Ar gas flow rate of 80 sccm. The deposition conditions used were as follows: target electrode bias voltage (−900 V) with direct current (3.1×10^{-2} A/cm^2); substrate bias voltage (−300 V) with impulse current (a pulse frequency and a duty cycle set at 1100 Hz and 85%, respectively); target/substrate distance of 10 mm; a deposition temperature of 800 °C and a deposition time of 3 h.

2.3. Microstructure characterization and mechanical tests

The phase composition of the as-deposited coatings was analyzed with a D8 ADVANCE X-ray diffractometer (XRD) using a Cu-Kα

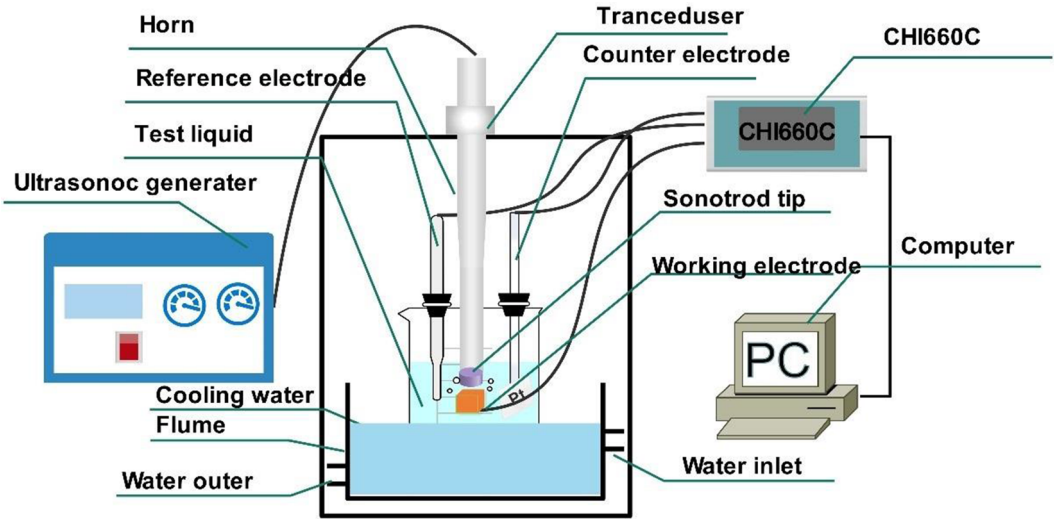

Fig. 2. Schematic of the ultrasonic cavitation erosion equipment.

(λ = 1.54056 Å) X-ray source (potential 35 kV and current 40 mA). The diffraction spectra were collected using Bragg-Brentano geometry. The tested specimens were examined with a scanning speed of 0.05° per second in a 2θ range of 20° to 80°. The surface and cross-sectional microstructures of the as-prepared coatings were studied using a field emission scanning electron microscope (FE-SEM, Hitachi, S-4800, Japan), equipped with an energy-dispersive X-ray analyzer (EDX-4; Philips). Detailed microstructural examination of the coatings was performed using a JEOL JEM-2010 transmission electron microscope (TEM) operating at an accelerating voltage of 200 kV. Plan-view TEM specimens were mechanically ground only from the untreated side of the substrate and then thinned to electron transparency using a single-jet electrochemical polisher.

Hardness and elastic modulus were measured on the coatings' surfaces using UMIS (Ultra-Micro Indentation System 2000, CSIRO, Sydney, Australia) workstation, A Berkovich diamond indenter was employed, which was applied at a constant loading rate of 20 mN/min with a maximum applied load of 20 mN. Hardness and the elastic modulus were calculated using the Oliver-Pharr method [18] derived from the measured load-displacement curves. For each specimen, ten measurements were conducted and the presented values are an average of 10 indentations. To examine the contact damage resistance of the coatings, the cross-sections of the indentations, generated by a spherical indenter with a radius of 5 μm, were examined using a dual beam focused ion beam (FIB) microscope. The adhesion strength between the coating and the substrate was measured quantitatively by means of a WS-97 scratch tester, which was equipped with an acoustic emissions (AE) sensor. During scratch tests, a conical Rockwell C diamond stylus with a 0.2 mm radius was drawn across the coating surface at a constant loading rate of 20 N/min and a scratching speed of 1 mm/min. The critical load (Lc), defined as the minimum normal load required for starting adhesion failure, was determined by both acoustic emission fluctuations and through SEM observation of the scratch tracks.

2.4. Electrochemical measurements and XPS analysis

Electrochemical measurements were undertaken in a standard three-electrode arrangement using a CHI 660C electrochemical workstation (Shanghai ChenHua Instruments Inc., China). The tests were carried out in a 0.5 M HCl solution using a saturated calomel reference electrode (SCE) and platinum plate counter electrode. Current-time response tests were conducted using a potential of +0.6 V_{SCE}. Potentiodynamic polarization measurements were undertaken with an electrode potential range from −0.5 to +1.5 V_{SCE} with a scan rate of 1 mV/s. The electrochemical impedance spectroscopy (EIS) experiments were performed at open circuit potential (OCP) using a perturbation amplitude of 10 mV over a frequency range from 100 kHz to 10 mHz. Then, the data acquired from EIS were analysed and modeled via an appropriate electrical equivalent circuit (EEC) using ZSimpWin software.

The composition and chemical valence states of the passive films formed on samples following corrosion testing were characterized by X-ray photoelectron spectroscopy (XPS) using a Kratos AXIS Ultra ESCA System, operating with an Al Kα X-ray source, with a 12 kV accelerating voltage and a 12 mA emission current. The base pressure of the sample chamber was ~10^{-10} Torr or better. The pass energy was chosen to be 80 eV for survey scans and 10 eV for feature scans. After subtraction of the background signals, the spectra were fitted using both Gaussian and mixed Gaussian/Lorentzian functions. Binding energies were calibrated using carbon contamination to the C1s peak value at 284.8 eV. The standard binding energies of the analyzed elements were determined from the NIST XPS database (V4.0).

2.5. Cavitation-erosion tests

The cavitation erosion tests were performed using a JY92-IIDN magnetostrictive-induced cavitation apparatus (NingBo Scientz Biotechnology Co., Ltd.) with a maximum output power from the ultrasonic generator of 1000 W. Tests were performed according to ASTM G32-16 [19]. Fig. 2 shows a schematic diagram of cavitation erosion equipment. During cavitation erosion testing, the samples were mounted on a support table that was was positioned 1 mm below the tip of a vibrating horn made of titanium alloy. Both the vibrating horn and the test samples were immersed in the test liquid in a 1000 ml glass beaker. This was maintained at 20 ± 1 °C by flowing cooling. The vibratory frequency and double vibratory amplitude were kept at 20 kHz and 60 μm, respectively. The total test period of each sample was 9 h and the tested samples were weighed periodically by an analytical balance with a sensitivity of 0.01 mg to determine mass loss.

3. Results and discussion

3.1. Calculation results

The structural stability of a compound, which is closely associated with its formation enthalpy, is of great importance to evaluate its alloying ability. The formation enthalpy (ΔH_f) was determined by subtracting the total energies of individual constituent atoms in their bulk structures from the total energy of the compounds. ΔH_f for $Ta(Si_{1-x}Al_x)_2$

Table 1
Calculated lattice constants and formation enthalpies for C40-structured $TaSi_2$ and Al-doped $Ta(Si_{1-x}Al_x)_2$.

$Ta(Si_{1-x}Al_x)_2$	Lattice constants(Å)		$\triangle H_f$ (eV/atom)
	a	c	
$TaSi_2$-This work	4.823	6.606	−0.588
$TaSi_2$-Ref. [20]	4.821	6.637	−0.542
$Ta(Si_{0.958}Al_{0.042})_2$	4.826	6.626	−0.585
$Ta(Si_{0.917}Al_{0.083})_2$	4.831	6.648	−0.581
$Ta(Si_{0.875}Al_{0.125})_2$	4.836	6.672	−0.578
$Ta(Si_{0.833}Al_{0.167})_2$	4.845	6.693	−0.571

compounds can be described by the following equation:

$$\Delta H_f = \frac{E_{tot}[Ta(Si_{1-x}Al_x)_2] - 12E(Ta) - 12(2-2x)E(Si) - 24xE(Al)}{36} \quad (1)$$

where $E_{tot}[Ta(Si_{1-x}Al_x)_2]$ refers to the total energy of the super cell for the $Ta(Si_{1-x}Al_x)_2$ compounds; E(Ta), E(Si) and E(Al) signify the energy per atom for Ta, Si and Al atoms in the solid state, respectively. The equilibrium lattice constants and formation enthalpies for C40 structured Ta $(Si_{1-x}Al_x)_2$ determined as a function of Al concentration are tabulated in Table 1, along with other available theoretical data [20]. From Table 1, it is clear that the calculated lattice constants and formation enthalpy for binary $TaSi_2$ are close to previously generated theoretical results, suggesting that the present calculations are both reasonable and reliable. As expected, both the calculated lattice parameters *a* and *c* increase simultaneously with increasing substitution of Al atoms for Si, as the atomic radius of aluminum is slightly larger than that of silicon. All of Ta $(Si_{1-x}Al_x)_2$ compounds have a negative formation enthalpy, showing that they are thermodynamically stable in the ground state. Moreover, the formation enthalpy calculations suggest that the addition of aluminum lowers the structural stability of $TaSi_2$, because the higher aluminum concentration has a more positive ΔH_f value.

Elastic properties of a solid, such as bulk modulus (B), Young's modulus (E), Shear modulus (G) and Poisson's ratio (υ), can help gain a deep understanding of its mechanical properties [21]. The elastic constants (C_{ij}), reflecting a solid's response to an external pressure, provide critical information to understand the elastic properties of compounds. According to the symmetry of hexagonal structured $TaSi_2$, there are five independent elastic constants: C_{11}, C_{12}, C_{13}, C_{33}, and C_{44}. Further, the elastic constant C_{66} has a connection with other constants as $C_{66} = (C_{11} - C_{12})/2$. Table 2 gives the calculated elastic constants of binary and ternary $TaSi_2$, together with the available theoretical data. Based on Born-Huang stability criteria, the elastic constants of hexagonal crystals need to satisfy the following inequalities [22]:

$$C_{12} > 0,\ C_{11} - C_{12} > 0,\ C_{33} > 0,\ C_{44} > 0,\ (C_{11} + C_{12})C_{33} > 2C_{13}^2 \quad (2)$$

Clearly, the calculated elastic constants for these compounds meet the Born-Huang stability criteria, indicating that both binary and ternary $TaSi_2$ are mechanically stable at the ground state. Furthermore, the calculated elastic constants of binary $TaSi_2$ are in strong agreement with the experimental and theoretical data reported by others [20,23]. It is obvious that the C_{33} values for all of the $Ta(Si_{1-x}Al_x)_2$ compounds are larger than the C_{11} values, suggesting that these compounds exhibit the higher deformation resistance along the c-axis directions in comparison with the a-axis direction under uniaxial stress. This may have resulted from the presence of strong Si-Si covalent bonds along the *c*-axis. With increasing Al concentration, the C_{33} values slightly decrease, implying that the Al additions weaken rigidity along the *c*-axis directions. For Al alloyed $TaSi_2$, a component of the Si-Si covalent bonds is replaced by Al-Si covalent bonds. Hence, this result also indicates that the strength of the formed Si-Al covalent bonds in Al alloyed $TaSi_2$ is weaker than that of the Si-Si covalent bonds along the c-axis. In addition, the elastic constant, C_{44}, indicates the resistance to monoclinic shear along the (1 0 0) plane. From Table 2, it is evident that the C_{44} values decrease with Al alloying, denoting a decrease in shear resistance along the (1 0 0) plane.

Table 2
Calculated elastic constants (Cij in GPa) of $Ta(Si_{1-x}Al_x)_2$, compared with available results.

$Ta(Si_{1-x}Al_x)_2$	C_{11}	C_{12}	C_{13}	C_{23}	C_{33}	C_{44}	C_{55}	C_{66}
$TaSi_2$-This work	350.8	70.4	77.8	78.2	466.6	148.8	147.1	140.2
$TaSi_2$-Ref. [20]	351.0	84.0	73.0		461.0	123.0		(133.5)
$TaSi_2$-Ref. [23]	375.3	78.4	90.1		476.7	143.7		148.5
$Ta(Si_{0.958}Al_{0.042})_2$	354.3	72.4	77.7	77.5	448.7	137.2	139.3	141.2
$Ta(Si_{0.917}Al_{0.083})_2$	354.8	68.8	77.1	77.5	438.8	131.1	133.6	143.8
$Ta(Si_{0.875}Al_{0.125})_2$	349.8	70.8	77.0	77.0	429.5	122.4	126.1	142.6
$Ta(Si_{0.833}Al_{0.167})_2$	351.3	69.3	73.5	69.5	424.8	114.9	118.2	142.4

In terms of the obtained C_{ij} values, the mechanical moduli of $Ta(Si_{1-x}Al_x)_2$ compounds with differing Al contents can be determined using the Voigt-Reuss-Hill approach, as shown in Fig. 3. Our calculated data for binary $TaSi_2$ are consistent with calculations by others [20], further confirming the reliability of our calculations. Bulk modulus (B) is associated with the ability of a material to resist crystal volume changes under hydrostatic pressure, whereas the shear modulus (G) describes the ability of a solid to resist shape change caused by a shearing force, whilst Young's modulus (E) reflects the degree of elastic stiffness for a solid [24]. From Fig. 3, it is clear that the values for bulk modulus (B), shear modulus (G) and Young's modulus (E) all decrease with increasing Al additions. This indicates that the addition of Al into $TaSi_2$ not only weakens the deformation resistance to volume and shear deformation, but also reduces elastic stiffness. It is important to note that Young's modulus is also regarded as the indicator of the nature of chemical bonding of a compound [25]. Predictably, the increase of Al addition reduces the covalent feature of these $Ta(Si_{1-x}Al_x)_2$ compounds.

Vickers hardness (H_V) represents the ability of a material to resist plastic deformation and thus plays an important role in material's selection, for example against wear. An empirical relationship between Vickers hardness and elastic modulus was proposed to estimate the hardness of polycrystalline materials through the following equation [26]:

$$H_V = 2(k^2G)^{0.585} - 3 \quad (3)$$

where k refers to the G/B ratio. This equation signifies that that Vickers hardness is more closely related to G/B ratio than either E or G alone, due to the G/B power index of 2. As shown in Fig. 3, the variation of H_V values with variations in Al additions is analogous to that for the B, G and E values. The calculated results show that Al additions result in solid solution softening for $TaSi_2$.

To better understand the influence of Al alloying on the brittle-or-ductile behavior of $TaSi_2$, we examined variations of Pugh ratio (B/G), Poisson's ratio (ν) and Cauchy pressure with Al concentrations in $TaSi_2$, as presented in Fig. 4. According to Pugh's rule, the ratio of the bulk modulus to shear modulus (B/G ratio) can acts as a parameter to indicate whether a material exhibits brittle or ductile behavior. In general, the larger the B/G ratio, the greater the degree of ductility. The critical value of B/G ratio, separating ductility from brittleness, is approximately 1.75. If B/G ratio > 1.75, a solid is expected to exhibit ductile behavior, and vice versa; if B/G ratio < 1.75, then a solid shows brittle behavior. As shown in Fig. 4, the B/G ratios for all the $Ta(Si_{1-x}Al_x)_2$ compounds are lower than the critical value, suggesting that those compounds exhibit brittle behavior. A clear increase in B/G ratio is observed when the Al concentration increases from 0 to 12.5 at.%, and the B/G ratio changes little with further increases in Al addition. This is due to the fact that shear modulus decreases much faster than bulk modulus when the Al concentration increases from 0 to 12.5 at.%, and the decreasing trend of shear modulus is comparable with that for bulk modulus, with a further increase in Al addition. Poisson's ratio (υ) is the rate of transversal

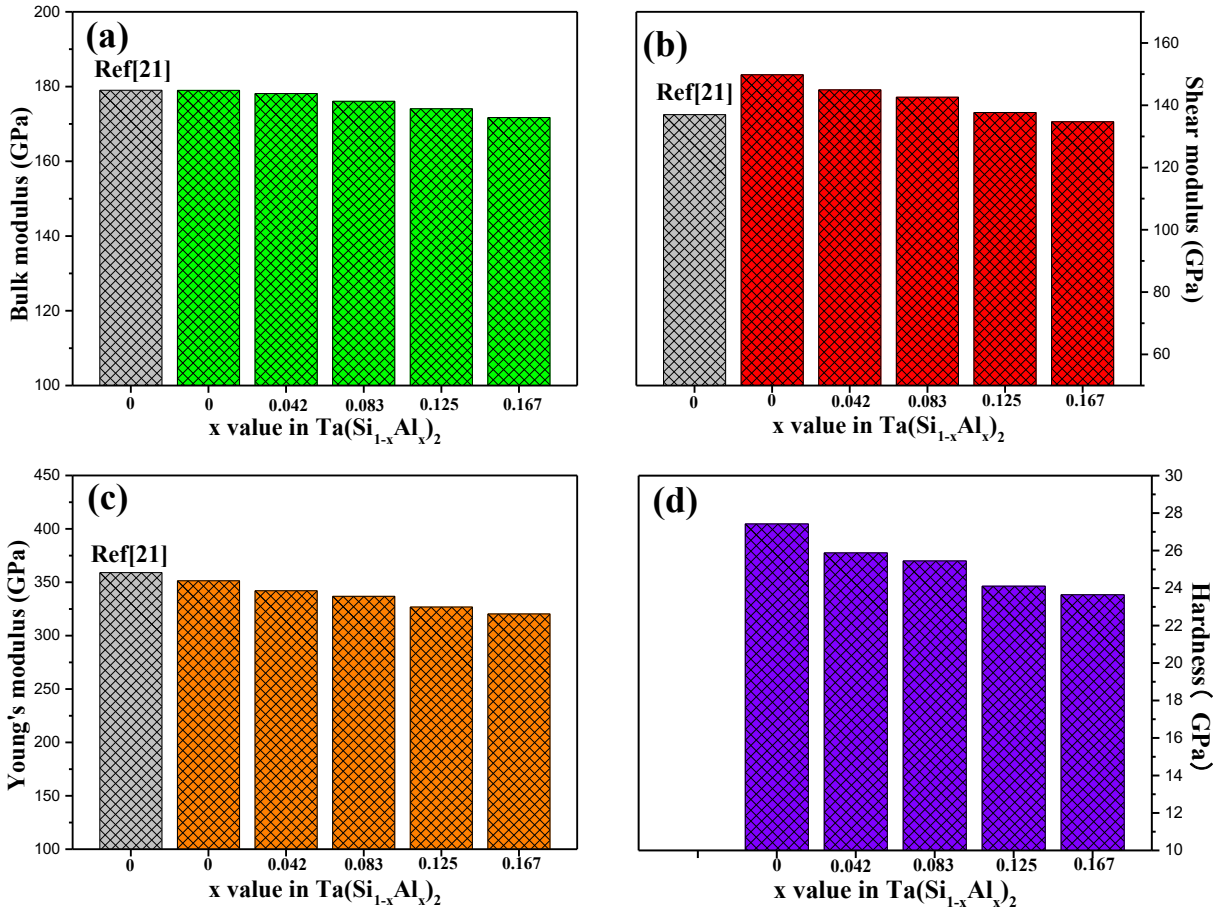

Fig 3. Calculated bulk moduli (a), shear moduli (b), Young's moduli (c) and hardness (d) for the $Ta(Si_{1-x}Al_x)_2$ compounds together with available theoretical values.

expansion or contraction divided by longitudinal contraction or extension, which usually ranges from −1 to 0.5. This parameter also reflects the covalent bonding character of a solid. Usually, if Poisson's ratio is greater than 0.26, a material possesses metallic characteristic and thus exhibits greater plasticity. The values for the Poisson's ratios for the five $Ta(Si_{1-x}Al_x)_2$ compounds are all smaller than 0.26, suggesting that they show strong covalent bond features, and the Al addition can improve the plasticity of $TaSi_2$ to some degree. Moreover, the Cauchy pressures, defined as $C'_{12} - C'_{44}$ for a hexagonal crystal ($C'_{12} = (C_{12} + C_{13} + C_{23})/3$, $C'_{44} = (C_{44} + C_{55} + C_{66})/3$), reveal the angular character of the atomic

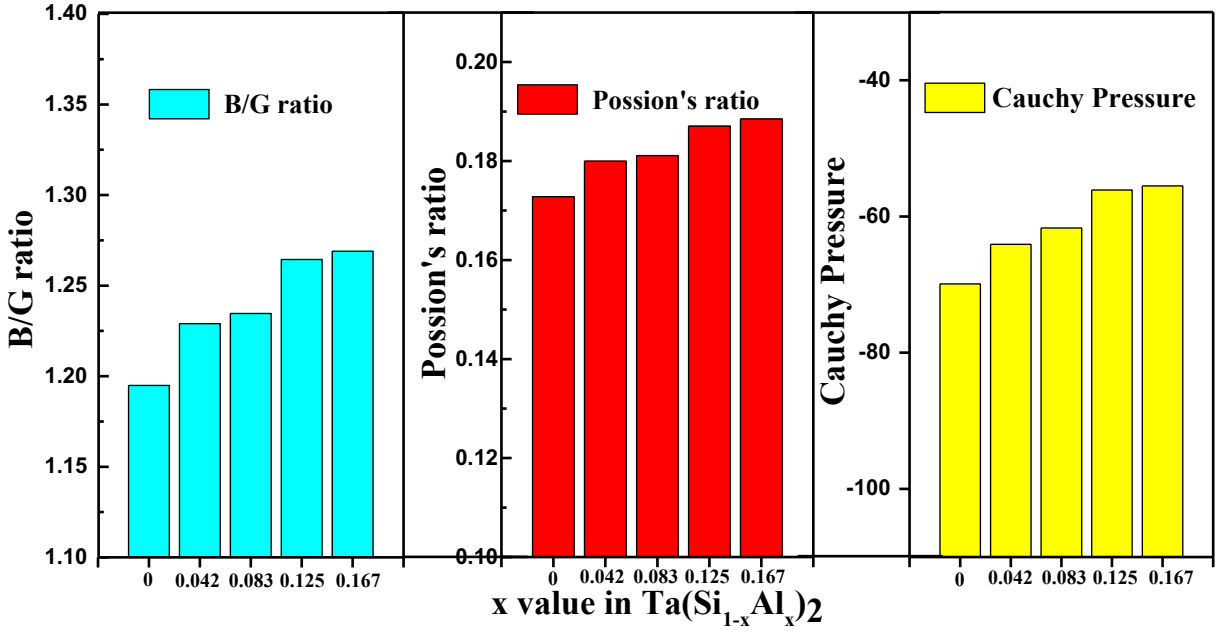

Fig 4. Calculated B/G ratio, Poisson's ratio (ν) and Cauchy Pressure for the $Ta(Si_{1-x}Al_x)_2$ compounds.

bonding features of a solid and this parameter has been also extensively used to characterize the brittleness or ductility of the solid [27]. A crystal that exhibits a positive Cauchy pressure is ductile with metallic bonding, otherwise it is brittle with directional covalent bonding. For the five Ta$(Si_{1-x}Al_x)_2$ compounds, the values of Cauchy pressures are negative, but increase with increasing Al concentration, indicating an enhanced ductility. Clearly, the variation of the B/G ratios, Poisson's ratios and Cauchy pressures of the Ta$(Si_{1-x}Al_x)_2$ compounds with Al concentration all shows a similar trend: a significant increase in plasticity as the Al content increases from 0 to 12.5 at.%, but a negligible change in plasticity with further additions of Al. Therefore, we chose Ta$(Si_{0.875}Al_{0.125})_2$ as an appropriate Al addition with which to prepare an alloyed $TaSi_2$ coating and then compare its mechanical behavior and corrosion response under cavitation erosion conditions with those of the binary compound and Ti-6Al-4V substrate.

3.2. Microstructural analysis

Fig. 5 presents typical X-ray diffraction spectra recorded from the two as-deposited Ta$(Si_{1-x}Al_x)_2$ (x = 0 and 0.125) coatings, in comparison with the standard JCPDS data (file No. 38-0483) for hexagonal C40 structured $TaSi_2$ (represented by vertical black lines). For the binary $TaSi_2$ coating, the diffraction peaks at 2θ values of 25.4°, 34.9°, 41.2°,60.8°and 74.5°, indexed to (1 0 1), (1 0 2), (0 0 3), (2 1 1) and (3 0 2) planes, respectively, that were consistent with the expected diffraction peaks for C40 structured $TaSi_2$. For the ternary Ta$(Si_{0.875}Al_{0.125})_2$ coating, no characteristic peaks of other Ta silicides are detected, indicating that no phase transition occurred after substitutional alloying with Al in this compound. Compared with the binary $TaSi_2$ coating, all the diffraction peaks for the Ta$(Si_{0.875}Al_{0.125})_2$ coating shift towards lower 2θ angles, presumably because the atomic radius of Al is bigger than that of Si. In addition, both patterns displayed relatively weak and broad peaks, arising from the very fine grain size of the two as-deposited coatings.

Fig. 6 shows typical cross-sectional SEM micrographs of the two as-deposited Ta$(Si_{1-x}Al_x)_2$ (x = 0 and 0.125) coatings, together with EDS elemental maps and energy dispersive X-ray point spectra from the coatings. From the cross-sectional SEM morphologies shown in Fig. 6, three distinct zones namely the Ta$(Si_{1-x}Al_x)_2$ coating, the substrate-coating interface and Ti-6Al-4V substrate could be distinctly observed along the depth from the top to the bottom of cross-sectional coated

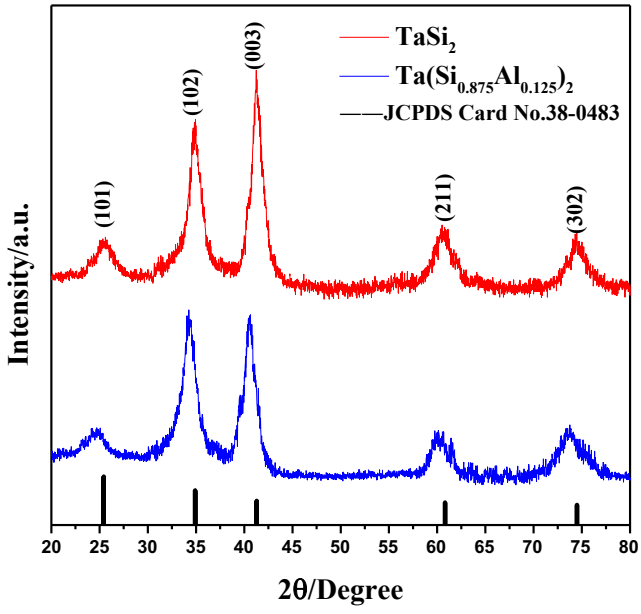

Fig 5. The XRD patterns for the as-deposited $TaSi_2$ and the Ta$(Si_{0.875}Al_{0.125})_2$ coatings.

samples. Both coatings have a uniform thickness of nearly 15 μm and exhibited a dense and homogeneous microstructure without cracking and delamination at the interface. Such a thick Ta$(Si_{1-x}Al_x)_2$ coating of good quality is desirable for protection of the metal substrate from mechanical and corrosion damage in the adverse circumstances. The elemental maps verify that Ta, Si and Al elements are homogeneously distributed throughout the coatings. EDS analysis of the coatings further revealed the presence of Ta, Si and Al (for the ternary coating) elements and Ta/Si or Ta/(Si + Al) atomic ratio was measured to be close to 0.5, consistent with the stoichiometry ratios for $TaSi_2$ and Ta$(Si_{0.875}Al_{0.125})_2$.

Fig. 7 presents typical planar view bright-field TEM and HRTEM images recorded from the Ta$(Si_{0.875}Al_{0.125})_2$ coating, along with corresponding selected area diffraction (SAD) pattern presented as an inset in Fig. 7(a). It is evident from Fig. 7(a) and (b) that the Ta$(Si_{0.875}Al_{0.125})_2$ coating is characterized by a uniform nanocrystalline grain structure. The grains are round in shape and appear equiaxed with an average diameter of ~5 nm, as evidenced by the high-resolution TEM image (Fig. 7(c)). As can be seen from the SAD pattern, the almost continuous rings with uniform intensity suggest that the coating exhibits an essentially random crystallographic texture. The three Debye-Scherrer rings (marked in the inset of Fig. 7(a)) were identified as the (1 0 2), (0 0 3) and (2 1 1) Bragg reflections of hexagonal $TaSi_2$, and no other crystalline phases were detected. This is consistent with the data obtained from XRD. We have employed an image quality enhancement program using Digital Micrograph software to analyze the high-resolution TEM image, as displayed on both the left and right sides in Fig. 7(c). It is evident from Fig. 7(c) that many spherical grains overlap with each other and the interlayer spacings of 2.56 Å and 2.19 Å, measured by Digital Micrograph software, correspond to the (1 0 2) and (0 0 3) planes, respectively, of hexagonal C40 structured $TaSi_2$. A similar microstructure also exhibiting a hexagonal structure was observed for the $TaSi_2$ coating.

3.3. Mechanical properties

Fig. 8 presents load versus depth (*P-h*) curves recorded on both the as-deposited Ta$(Si_{1-x}Al_x)_2$ (x = 0 and 0.125) coatings and uncoated Ti-6Al-4V under a maximum load of 20 mN. It is apparent that the maximum penetration depths of the two coatings are significantly lower than 10% of their coating thickness and thus the contribution from the underlying substrate to the measured mechanical properties is negligible. As expected, under the same maximum load, both coatings exhibit smaller indentation depths and less steep unloading slopes than the uncoated Ti-6Al-4V. This suggests that the uncoated alloy undergoes significantly more plastic deformation than the two Ta$(Si_{1-x}Al_x)_2$ coatings. The hardness values of the $TaSi_2$ and Ta$(Si_{0.875}Al_{0.125})_2$ coatings measured from the *P-h* curves, determined by Oliver and Pharr method, are 24.92 ± 0.82GPa and 23.09 ± 0.75GPa, respectively, which are about 4.4 and 4.1 times, respectively, greater than that of uncoated Ti-6Al-4V which exhibited a hardness value of 5.69 ± 0.41GPa. Likewise, the values for the Young's modulus of the $TaSi_2$ and Ta$(Si_{0.875}Al_{0.125})_2$ coatings are about 3.3 and 2.9 times higher than that of uncoated Ti-6Al-4V alloy, respectively. It is important to note that the values for hardness and Young's modulus for the binary $TaSi_2$ coating are much higher than those reported elsewhere. For example, the hardness of nanostructured $TaSi_2$, with an average grain size of 60 nm, was reported to be 13GPa) [28] and a bent $TaSi_2$ fiber was observed to exhibit a hardness of 11 GPa and a Young's modulus of 251 GPa) [29]. This higher hardness was also observed on other nanostructured metal silicides coatings reported in our previous studies, which was attributed to the finer grain size and denser microstructure [30]. Al alloying lowers the values of both hardness and Young's modulus of the $TaSi_2$ coating. This is consistent with the data obtained from first-principles calculations. During nanoindentation, the total deformation energy (W_t) induced by the indenter can be divided into two parts: energy dissipation of plastic deformation (W_p) and elastic recovery energy (W_e). The total deformation energy can be evaluated by the area enclosed by the loading plot and the maximum penetration

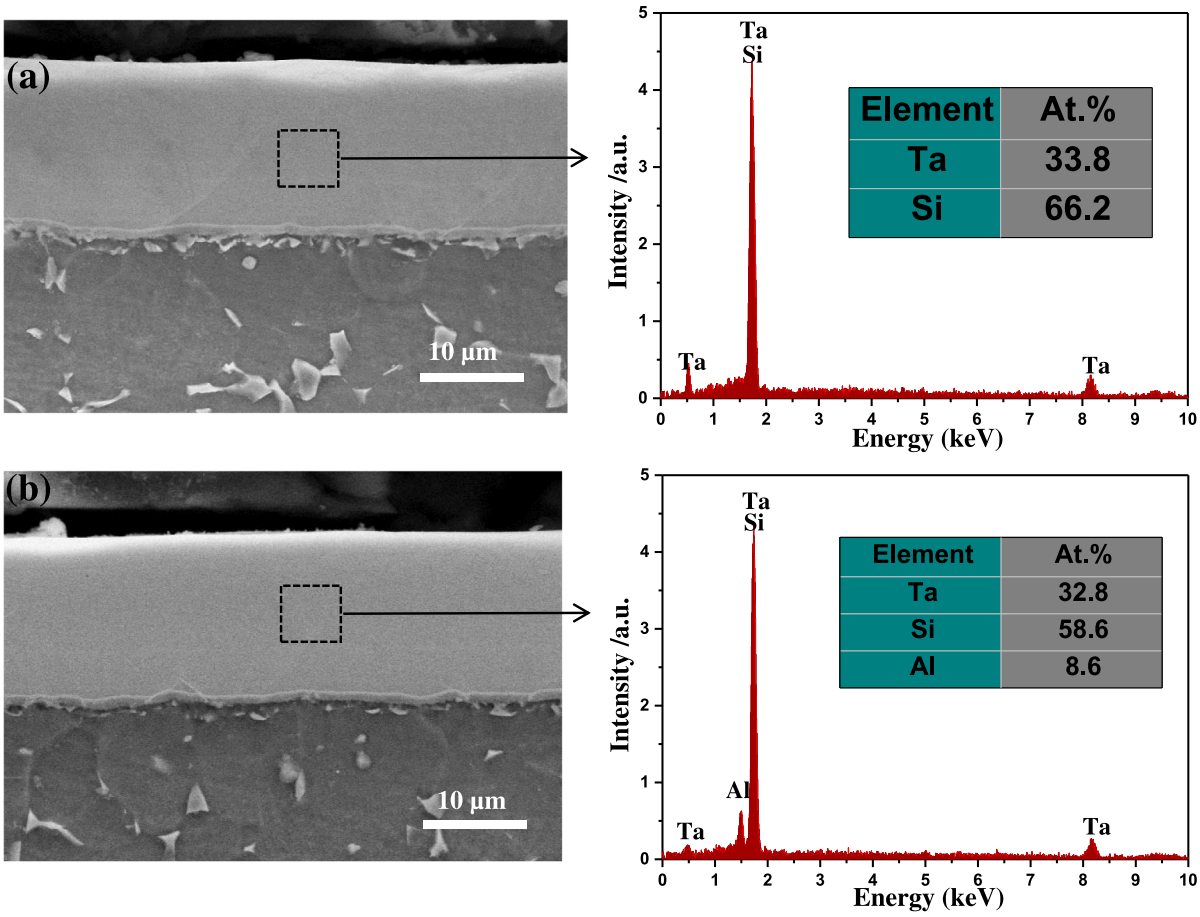

Fig. 6. Cross-sectional SEM images with the corresponding EDS point spectra for (a) $TaSi_2$ coating (b) $Ta(Si_{0.875}Al_{0.125})_2$ coating.

depth, while the elastic recovery deformation energy can be evaluated by the area enclosed by the unloading plot and the maximum penetration depth. The ratios of W_e/W_t and W_p/W_t represent the contribution of elasticity and plasticity to total deformation, respectively [31]. As shown in Fig. 8(d), the $Ta(Si_{0.875}Al_{0.125})_2$ coating has a higher W_p/W_t ratio than the $TaSi_2$ coating, indicating that Al addition enhances the plasticity of the $TaSi_2$ coating. Fig. 8(e) shows the H/E and H^3/E^2 ratios calculated using the measured values of E and H for the two $Ta(Si_{1-x}Al_x)_2$ coatings. Clearly, these ratios are approximately equal for the two coatings.

To investigate the influence of Al addition on the deformation behavior of the $TaSi_2$ coating, Vickers indentations were carried out on both coatings using different indentation loads ranging from 100 g to 1000 g with a 15 s dwell time, as shown in Fig. 9(a) and (b). Apparently, both coatings exhibit a plasticity-dominated response to indentation, with no evidence of radial cracking emanating from the indentation corners under an applied load. Owing to the absence of similar reported studies for $TaSi_2$ we compared the results of the two $Ta(Si_{1-x}Al_x)_2$ coatings with other metal silicides. Previous studies have shown that cracks were present at the corners of the indent impression for coarse grained binary silicides, such as $MoSi_2$ [32], Mo_5Si_3 [33] and Cr_3Si [34], and a $MoSi_2$-SiC nanocomposite [35], when they are subjected to indentation loads less than or equal to 1000 g. Hence, in comparison with these metal silicides, the two $Ta(Si_{1-x}Al_x)_2$ coatings studied here show higher toughness, since they require larger deformation energy for crack formation. In addition, after applying an indentation load of 1000 g, the same characteristic circular patterns surrounding the edges of the indent impression were seen on both coatings. Such patterns are actually slip-step patterns from shear bands, associated with the circular stress distribution induced by a Vickers indenter [36]. This deformation mode is frequently found on bulk metallic glasses (BMG) materials subjected to indentation [37]. As described earlier, both coatings exhibit ultrafine crystallites with a mean grain size of ~5 nm. Because of the lack of dislocation activity in such fine grain materials, the dominant deformation mechanism at room temperature is through shear sliding between the $Ta(Si_{1-x}Al_x)_2$ grains, which to some extent resembles deformation in BMG's. Fig. 9(c)–(f) shows plan-view images FIB cross-sections through indents on both coatings made under a normal load of 500 mN using a spherical indenter with a radius of 5 μm. The shape of the indentations on both coatings shows a round geometry in the plan-view images with no cracking observable on either the surface or cross-section of the indents. The $Ta(Si_{0.875}Al_{0.125})_2$ coatings exhibit larger projected indentation area and deeper non-recoverable indentation depth than those for the binary $TaSi_2$ coating, indicating that the binary $TaSi_2$ coating is harder. This is consistent with the values obtained using nanoindentation (Fig. 8). A number of researchers [38–40] have reported that sub-surface cracks can be observed underneath spherical indents applied using a 500 mN load on monolithic TiN coatings or TiSiN/TiN multilayer coatings. Consequently, these $Ta(Si_{1-x}Al_x)_2$ coatings show higher capability to accommodate deformation as compared to these TiN-based coatings.

Fig. 10 shows the acoustic emission signal intensity of the two $Ta(Si_{1-x}Al_x)_2$ coatings as a function of applied normal load, together with the corresponding scanning electron microscope images of the scratch tracks (see inset). During the scratch tests, the critical load (L_c) is defined as the minimum value load needed to remove the as-deposited coating from the substrate. As shown in Fig. 10, it is evident that the starting point for the occurrence of continuous acoustic emission is observed at applied loads of 46 N and 57 N for the $TaSi_2$ coating and $Ta(Si_{0.875}Al_{0.125})_2$ coating, respectively. The SEM images of the scratch morphologies suggest that the width of the scratch tracks increases with increasing the applied normal load, and large-scale spalling on both sides of the scratch tracks is observed once the critical load is attained. These results demonstrate that the $Ta(Si_{0.875}Al_{0.125})_2$ coating exhibits

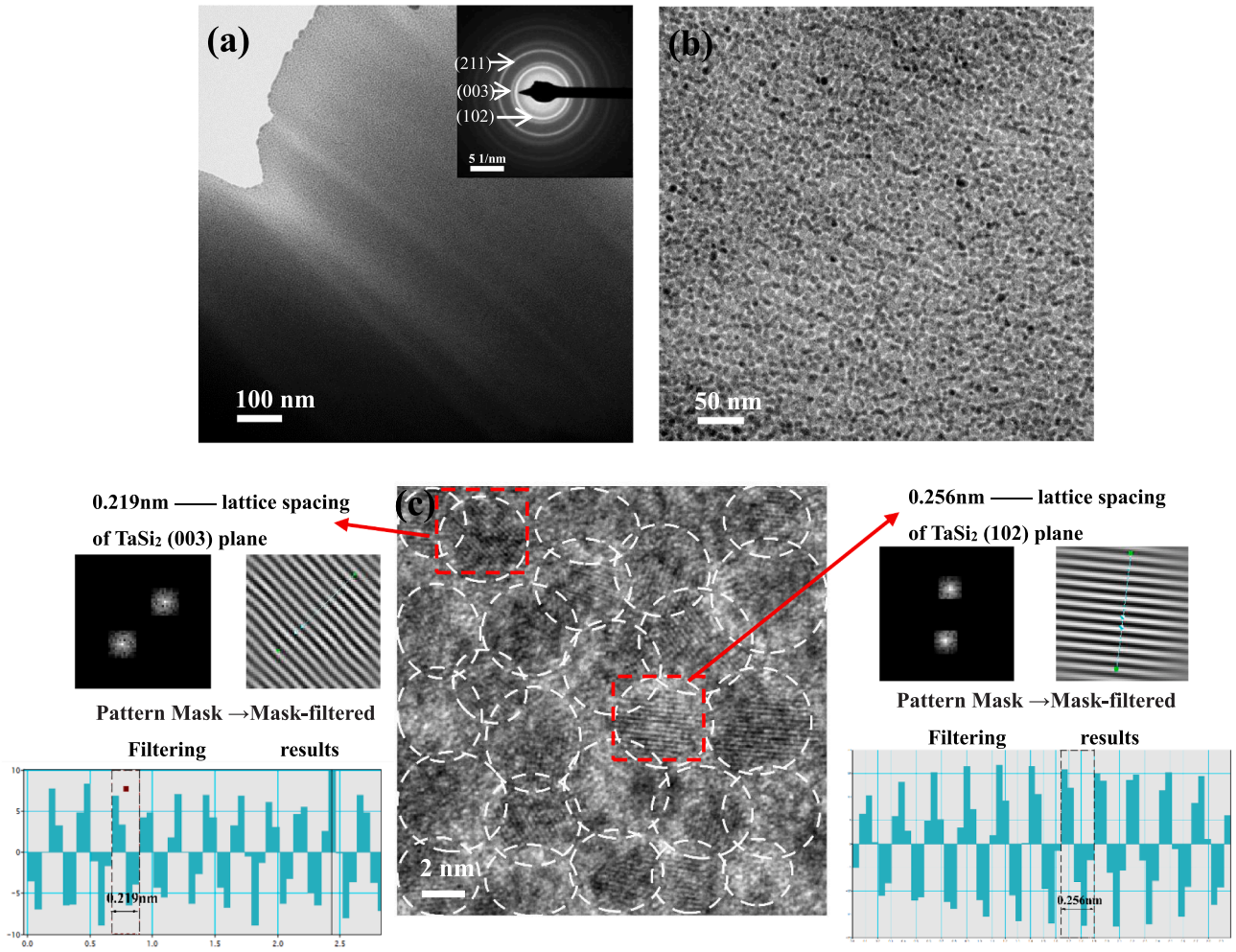

Fig.7. (a) a typical plan-view bright-field TEM image of the $Ta(Si_{0.875}Al_{0.125})_2$ coating , with (inset) the corresponding selected area diffraction (SAD) pattern and (b) a high-magnification image of the selected region in (a); (c) A high-resolution electron microscopy (HRTEM) image of the $Ta(Si_{0.875}Al_{0.125})_2$ coating.

superior in adhesion strength to the $TaSi_2$ coating. This is crucial to the reliability of the coating under hostile working conditions.

3.4. Cavitation erosion properties

3.4.1. Open circuit potential (OCP)/current-time responses

Under quiescent and ultrasonic cavitation conditions, the changes of the open circuit potential (E_{OCP}) registered for the two $Ta(Si_{1-x}Al_x)_2$ coatings and uncoated Ti-6Al-4V at different output powers in a 0.5 M HCl solution are shown in Fig. 11(a), where the output powers versus cavitation exposure time plot is displayed in Fig. 11(b). Under quiescent condition, the E_{OCP} for the three samples moves slowly to the noble direction. This shift of E_{OCP} is usually attributed to the formation of protective passive films on those tested samples. In contrast, when a cavitation measurement is to be initiated, the E_{OCP} of the tested samples shifts rapidly towards the cathodic direction. For the uncoated alloy, with increasing output powers, the E_{OCP} instantly decreases. In the case of the two coatings, the E_{OCP} almost maintains constant, being independently of the output powers. The influences of cavitation erosion on the E_{OCP} are determined primarily by two competing processes. The formation and subsequent collapse of cavitation bubbles induced by the transducer vibrations increase mass transport of oxygen, leading to a noble shift of the E_{OCP}. On the other hand, the repeated collapse of cavitation bubbles may cause the rupture of any spontaneously formed passive films on the tested samples and, thus, the underlying fresh surfaces are exposed to corrosive medium by the mechanically depassivation, resulting in a drop in E_{OCP}. In our case, the latter process plays a predominant role in cavitation tests at applied output powers ranging from 400 to 800 W. Such an active shift of the E_{OCP}, created by cavitation bubbles, has also been observed by other researchers [41]. Alternatively, an obvious E_{OCP} oscillation can be clearly observed on the E_{OCP} versus time curves for the tested samples. This is generally attributed to the depassivation/repassivation events, which occurred on the small regions of the tested samples [42]. Compared with the uncoated alloy, the amplitude of vertical oscillations in the E_{OCP} is markedly reduced, suggesting that the passive films formed on the two coatings exhibit a higher self-healing capability. The E_{OCP} of the $Ta(Si_{0.875}Al_{0.125})_2$ coating is greater than that of the $TaSi_2$ coating, indicating that Al addition further enhances the thermodynamic stability of the passive film present on the $TaSi_2$ coating. Fig. 11(c) shows the corresponding current-time transient plots recorded for the two $Ta(Si_{1-x}Al_x)_2$ coatings and uncoated Ti-6Al-4V potentiostatically polarized at potential of $+0.6\ V_{SCE}$ in a 0.5 M HCl solution under different output powers. The potential of $+0.6\ V_{SCE}$ employed here is located in the passive region observed from potentiodynamic polarization curves of the tested sample, as described in the following sections. For the uncoated alloy, in absence of cavitation, its current density is very stable; when cavitation is present, its current density rises sharply with increasing output powers, accompanied by large and continuous fluctuations in current. On the contrary, the application of cavitation does not appreciably affect the current density of the two coatings, especially for the $Ta(Si_{0.875}Al_{0.125})_2$ coating, which has a smoother current-time plot as compared to the $TaSi_2$ coating.

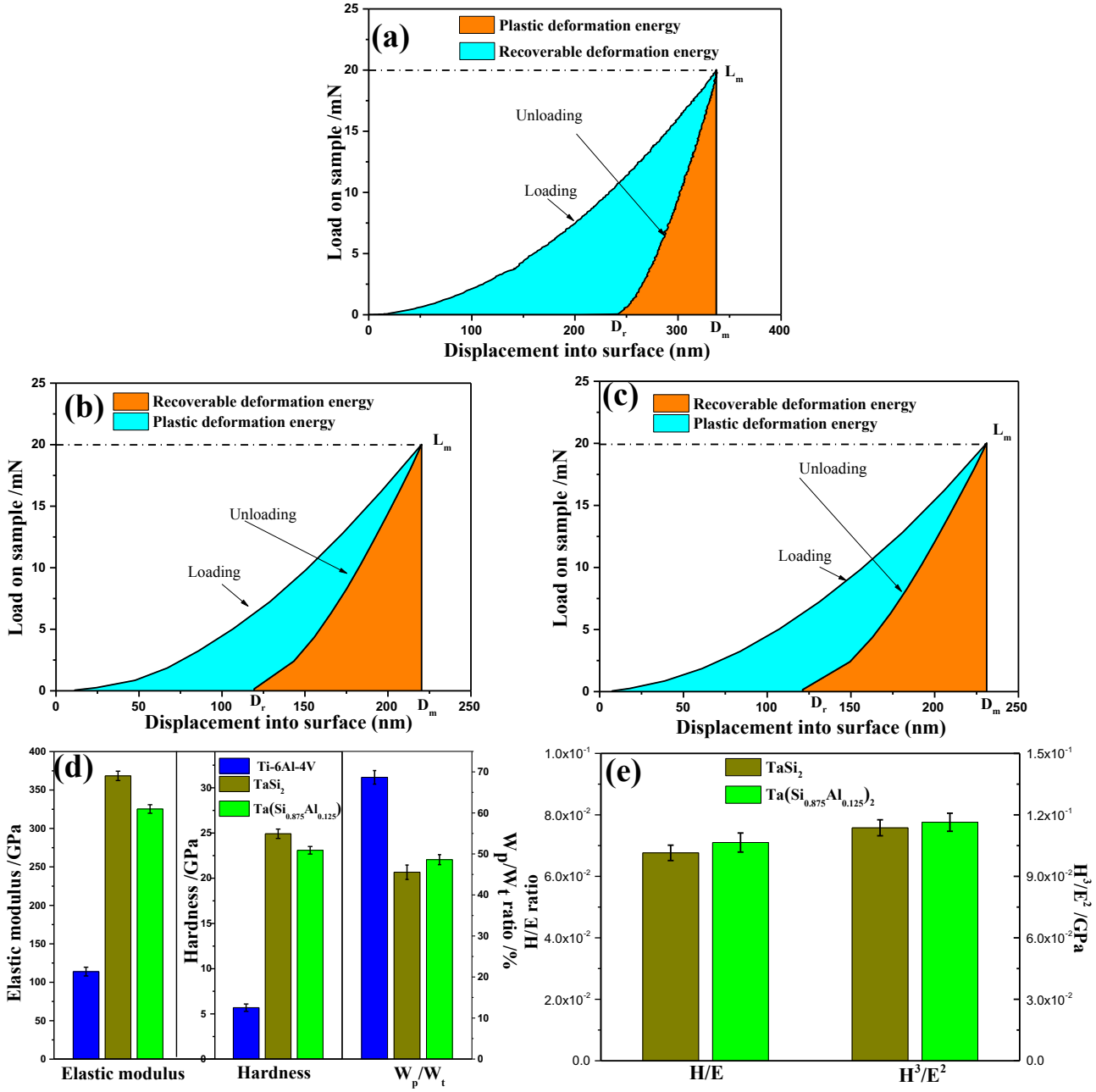

Fig. 8. Load-displacement curves for (a) Ti-6Al-4V alloy, (b) $TaSi_2$ coating and (c) $Ta(Si_{0.875}Al_{0.125})_2$ coating; (d) Young's modulus values, hardness and W_p/W_t ratio for the two coatings and uncoated Ti-6Al-4V; (e) the H/E and H^3/E^2 ratio for the two coatings.

3.4.2. Potentiodynamic polarization measurements

Fig. 12 shows typical potentiodynamic polarization curves of the two $Ta(Si_{1-x}Al_x)_2$ coatings together with bare Ti-6Al-4V in a 0.5 M HCl solution after different cavitation exposure times under a given output power of 800 W. All of the tested samples were polarized up to an anodic potential of +1.5 V_{SCE} to examine their passive nature. Table 3 gives the electrochemical parameters describing the polarization behavior, including corrosion potential (E_{corr}), corrosion current density (I_{corr}), and anodic/cathodic Tafel slopes (βa and −βc) extracted from polarization curves. As shown in Fig. 12, with increasing cavitation exposure time, a marked upwards displacement in cathodic branches is observed for the tested samples, meaning that the cathodic current densities rise continuously by prolonging cavitation time. For the hydrochloric acid medium used here, the cathodic reactions are mainly controlled by reduction of hydrogen ions and dissolved oxygen at the sample/solution interface. Hence, an increase of cavitation time accelerates the cathodic reactions process and speeds up the cathodic reaction rate. The anodic branches of the tested samples exhibit spontaneous passivation after different cavitation time, without exhibiting any active-passive transition. Analogous to the E_{OCP}/current-time curves, all the anodic branches show wide current oscillations, and gradually drift to higher anodic current density zones, with increasing cavitation time. Upon anodic polarization, the tested samples' surfaces undergo electrochemical dissolution and corrosion products form by anodic oxidization. With increasing cavitation time, the formed passive film becomes less protective and thinner due to the mechanical impact caused by the collapse of bubbles and the anodic dissolution was accelerated by more active sites exposed for corrosive attack [43]. As a result, the passivation current densities of the tested samples increase due to the prolonged interaction of the H^+ and Cl^- ions present in the 0.5 M HCl solution with the passive films formed on the tested specimens. From Table 3, it is observed that the anodic Tafel slopes (βa) are bigger than the cathodic counterparts (−βc) for the tested samples at a given cavitation

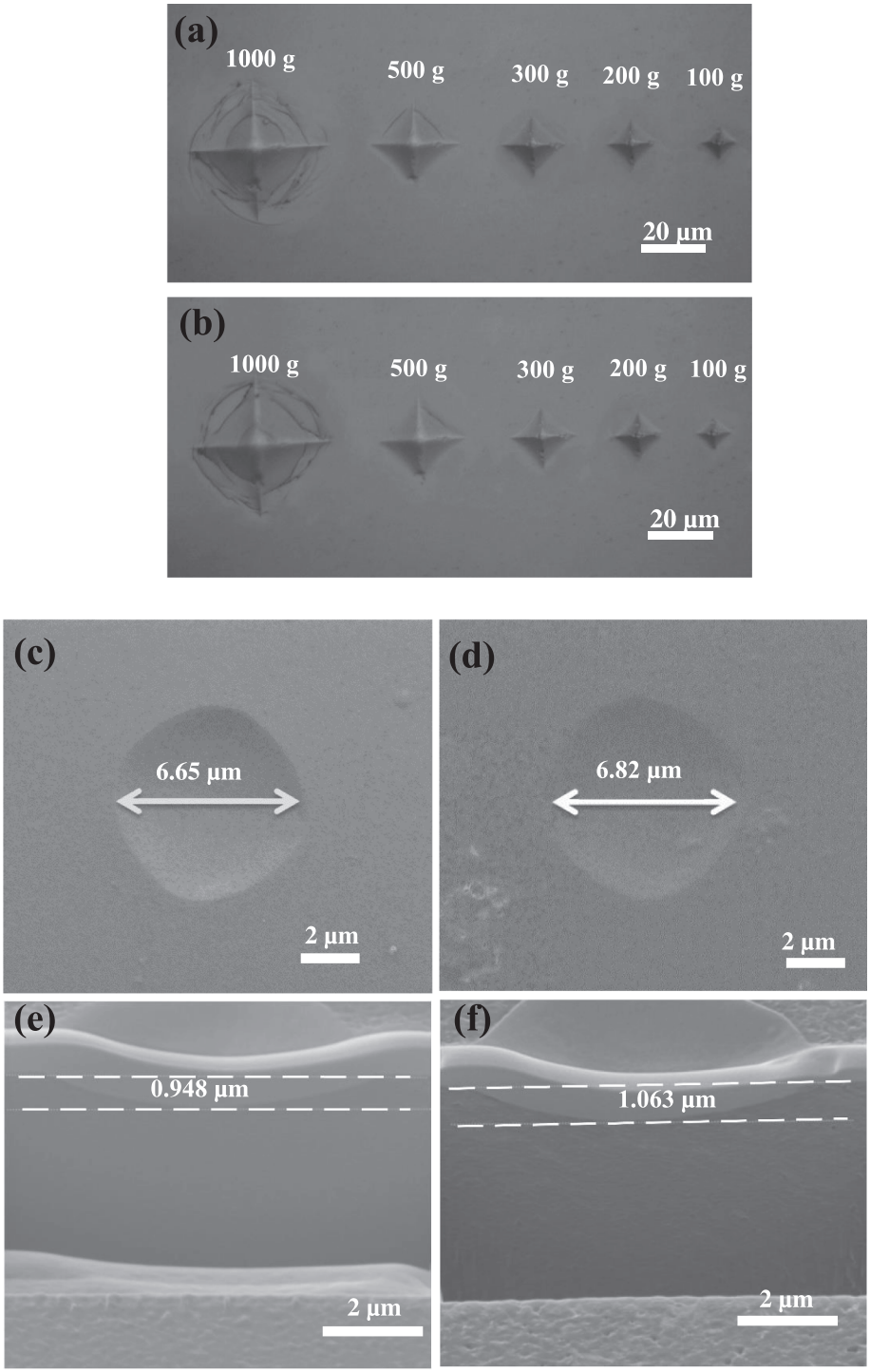

Fig. 9. Optical micrographs of Vickers indentations in (a) $TaSi_2$ and (b) $Ta(Si_{0.875}Al_{0.125})_2$ coating at applied loads ranging from 100 g to 1000 g; Images of the indentation impressions in the two coatings subjected to a load of 500 mN with a 5 μm radius spherical indenter. The plan view images: (c) $TaSi_2$ coating, (d) $Ta(Si_{0.875}Al_{0.125})_2$ coating; and cross-sectional SEM images: (e) $TaSi_2$ coating, (f) $Ta(Si_{0.875}Al_{0.125})_2$ coating.

time. This denotes that the overall kinetics of cavitation corrosion for the two $Ta(Si_{1-x}Al_x)_2$ coatings and uncoated alloy in a 0.5 M HCl solution are under anodic control, that is, the existence of the passive films grown on the tested samples. As shown in Table 3, with an increase of cavitation time, the E_{corr} values for the two coatings shifts towards more negative values, while the E_{corr} for the uncoated alloy tends to move towards more positive values. As the cavitation time is extended from 0 to 9 h, the anodic and cathodic branches of the tested samples shift following the order $a^1 \rightarrow a^2 \rightarrow a^3 \rightarrow a^4$ and $c^1 \rightarrow c^2 \rightarrow c^3 \rightarrow c^4$, respectively, and the corresponding E_{corr} changes in the following order E1 corr → E2 corr → E3 corr → E4 corr. For the uncoated alloy, the displacement of the cathodic branches to more positive potential region is more pronounced than that of the anodic branches moving to the lower potential region. Contrary to the uncoated alloy, a marked leftward displacement to lower potential region in the anodic branches of the two coatings is observed. Such variations explain why different E_{corr} shifts are observed on both coatings and bare Ti-6Al-4V. The values of i_{corr} for the tested samples increase with cavitation time, suggesting a reduction in the protective properties of the passive films

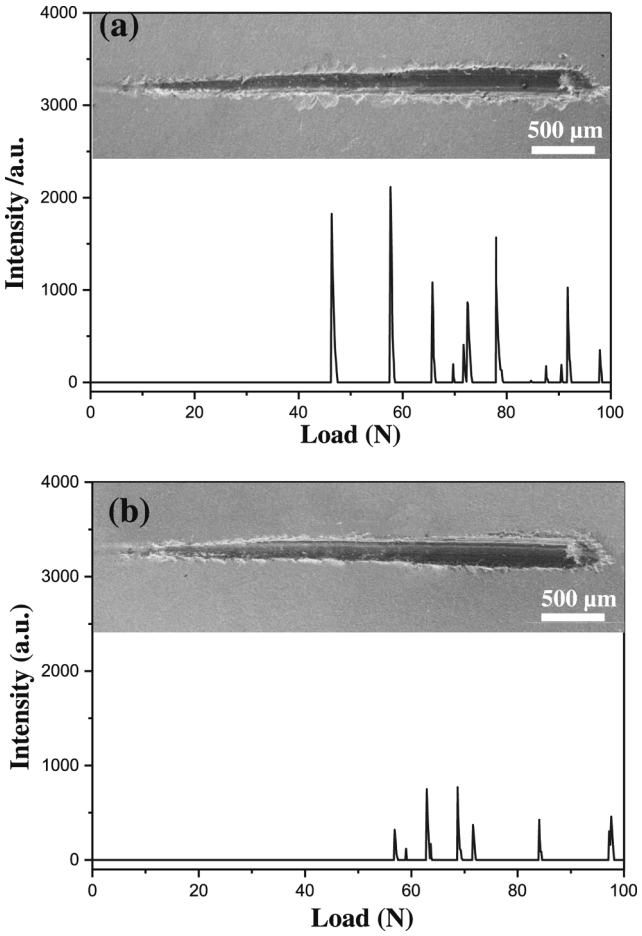

Fig. 10. SEM images of the scratch track and acoustic emission signal peaks versus normal load curves for (a) the $TaSi_2$ coating and (b) the Ta $(Si_{0.875}Al_{0.125})_2$ coating.

formed. At a given cavitation time, the i_{corr} values decrease in the sequence: uncoated Ti-6Al-4V > binary $TaSi_2$ coating > $Ta(Si_{0.875}Al_{0.125})_2$ coating. This result indicates a higher protective capacity of the Ta $(Si_{0.875}Al_{0.125})_2$ coating in comparison with those of uncoated Ti-6Al-4V alloy or the binary $TaSi_2$ coating.

3.4.3. Electrochemical impedance spectroscopy (EIS) measurements

Fig. 13 displays the impedance spectra of the two $Ta(Si_{1-x}Al_x)_2$ coatings and uncoated Ti-6Al-4V as Nyquist plots/Bode plots versus cavitation time in a 0.5 M HCl solution under a given output power of 800 W. Under the quiescence condition, the Nyquist plots of the test samples exhibit single, large unfinished capacitive semi-circle over the entire frequency range and the corresponding Bode-phase plots are typical of passive character, characterized by a broad frequency range with a maximum near −90° [44]. These results indicate that the passive films formed on the tested samples under static conditions show a strong capacitive behavior and endow the tested specimens with large electrochemical reaction resistance. In this case, impedance spectra registered for the tested samples is composed of only single time constant, and thus a modified Randles circuit ($R_s((Q_pR_p))$ was proposed to fit the impedance data, as shown in Fig. 14(a). In this equivalent circuit, a parallel combination of a resistor, R_p, representing the resistance of passive films, and a capacitor, Q_p, representing the capacitance of the passive films, are in series with a resistor, R_s, representing the solution resistance. For ultrasonic cavitation conditions, the capacitive loops in the Nyquist plots become more depressed and the diameters of the capacitive arcs decrease with increases in cavitation exposure time, implying that the protective ability of the passive films formed on the

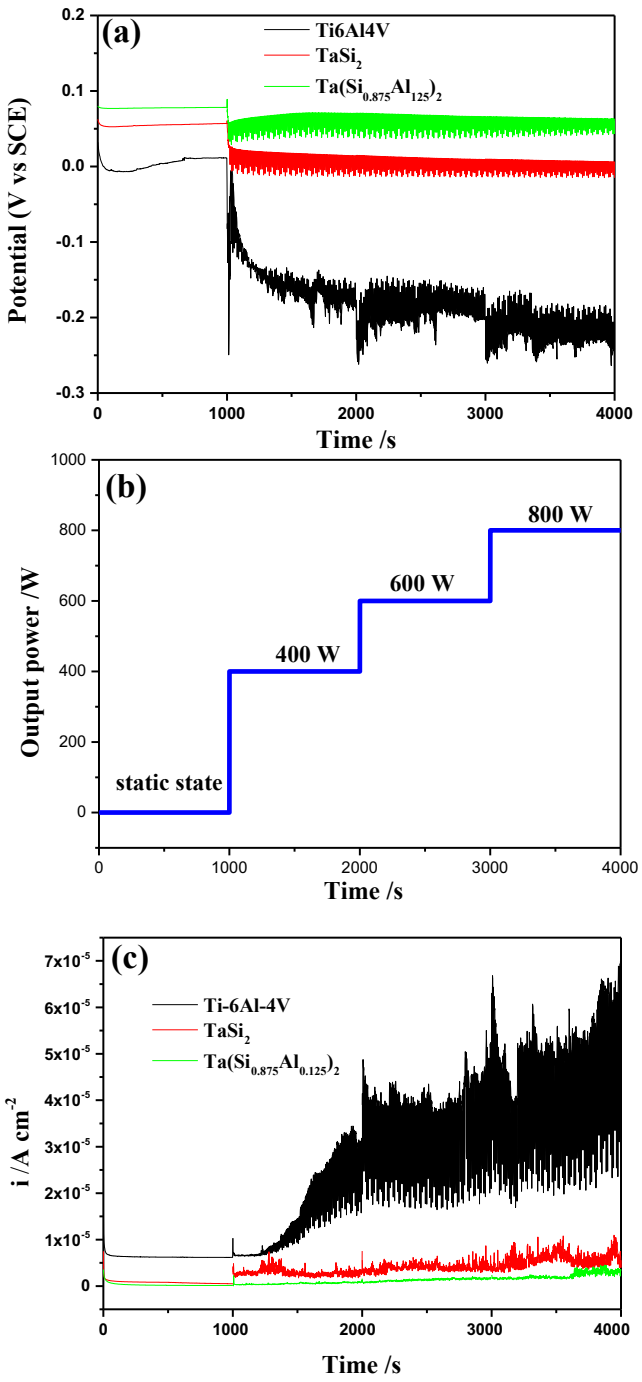

Fig. 11. (a) the open circuit potential (OCP)-time curves for samples tested in a 0.5 M HCl solution with different output powers; (b) the electrical output powers as a function of exposure time; (c) the current densities for tested samples as a function of the electrical output powers at a constant potential of +0.6 V_{SCE} in a 0.5 M HCl solution.

tested samples is decreased with increasing cavitation exposure time. From the Bode-phase plots, it is evident that there are two distinct phase angle peaks located in the high and low frequency parts for the uncoated alloy and binary $TaSi_2$ coating under ultrasonic cavitation erosion conditions. An equivalent circuit with two time constants, given in Fig. 14(b), was used to fit the experimental EIS data obtained from uncoated alloy and binary $TaSi_2$ coating after different cavitation times. From the literature, the two time constants are relevant to the generation of a passive film with bilayer architecture, that consists of a more protective, inner, dense layer with a lower frequency time

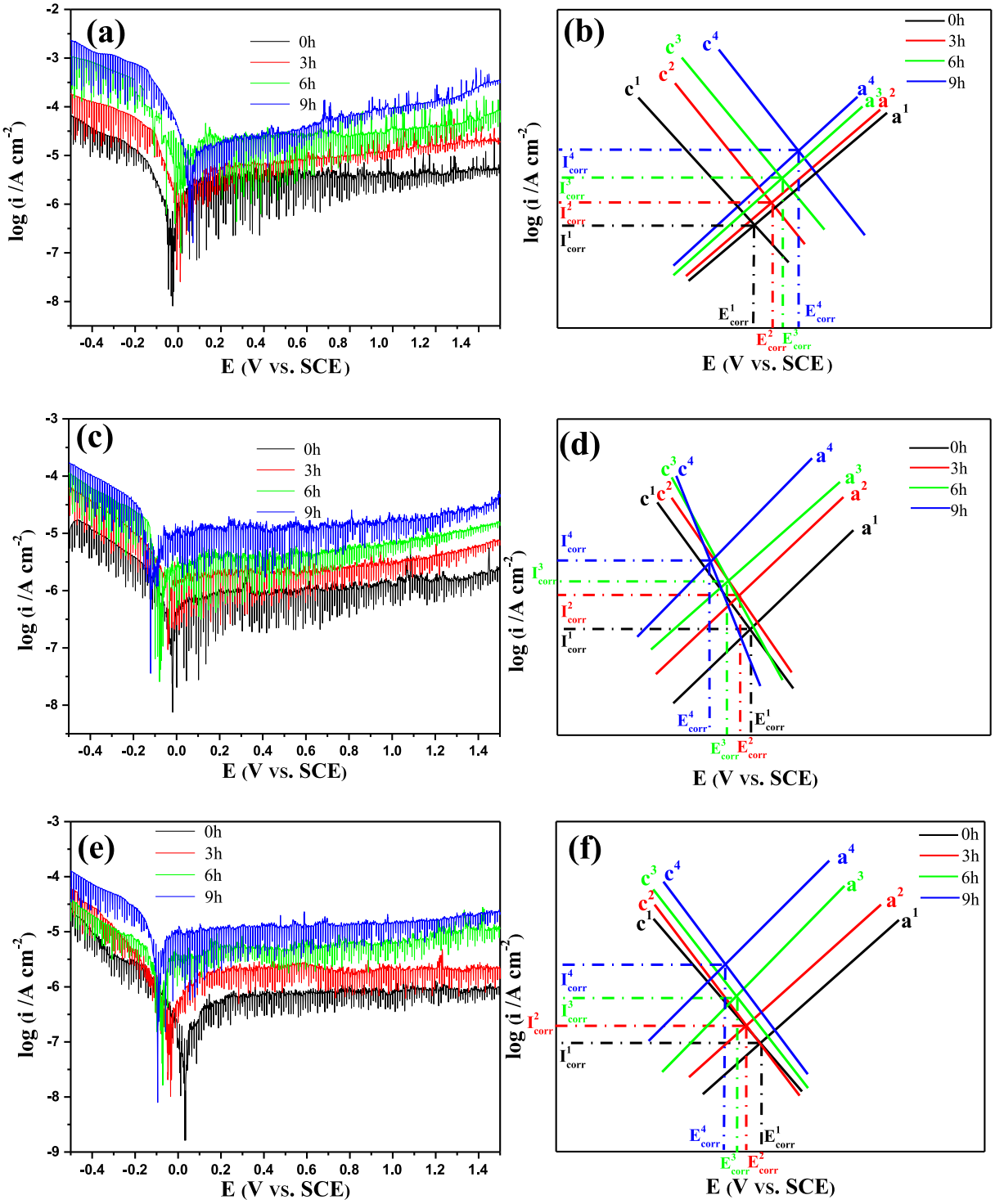

Fig. 12. The potentiodynamic polarization curves and the ideal schematic mechanism of the anodic and cathodic polarization curves for (a) and (b) Ti-6Al-4V, (c) and (d) the $TaSi_2$ coating, (e) and (f) the $Ta(Si_{0.875}Al_{0.125})_2$ coating in a 0.5 M HCl solution after different intervals of ultrasonic cavitation erosion with the output power of 800 W.

constant and a porous and non-protective outer layer with a higher frequency time constant [45]. In this equivalent circuit ($R_s(Q_pR_p)(Q_bR_b)$) comprises two capacitive/resistive elements in series, among which R_b and Q_b represent the resistance and capacitance of the inner dense layer, and R_p and Q_p represent the resistance and capacitance of the outer porous layer. In the case of the $Ta(Si_{0.875}Al_{0.125})_2$ coating, the impedance spectra obtained from 3 h of exposure were fitted using a ($R_s((Q_pR_p))$ model shown in Fig. 14(a) and the ($R_s(Q_pR_p)(Q_bR_b)$) model shown in Fig. 14(b) was employed to simulate the experimental impedance data obtained from 6 h and 9 h of exposure. Table 4 summarizes the calculated equivalent circuit parameters derived from fitting the EIS experimental data of the tested samples. The chi-square (χ^2) values were of the order of 10^{-3}–10^{-4} that suggests the validity of the proposed circuit models. Under the quiescence condition, the R_p value increases from $4.62 \times 10^6\ \Omega\ cm^2$ for the uncoated alloy to $8.52 \times 10^6\ \Omega\ cm^2$ for the binary $TaSi_2$ coating and further to

Table 3
Polarization parameters of the two coatings and uncoated Ti-6Al-4V under different cavitation times.

	Cavitation Time	E_{corr} (V_{SCE})	i_{corr} (Acm^{-2})	β_a (mV/decade)	$-\beta_c$ (mV/decade)
Ti-6Al-4V	0 h	−0.029	1.34×10^{-6}	348.8	91.7
	3 h	0.010	3.73×10^{-6}	327.2	78.7
	6 h	0.012	8.65×10^{-6}	311.8	71.5
	9 h	0.069	1.28×10^{-5}	292.2	69.2
$TaSi_2$	0 h	0.011	7.03×10^{-7}	383.9	158.3
	3 h	−0.040	9.41×10^{-7}	333.3	149.3
	6 h	−0.075	2.94×10^{-6}	301.4	141.7
	9 h	−0.103	7.08×10^{-6}	285.4	130.2
$Ta(Si_{0.875}Al_{0.125})_2$	0 h	0.035	3.27×10^{-7}	442.2	168.3
	3 h	−0.065	6.30×10^{-7}	389.8	176.4
	6 h	−0.071	1.52×10^{-6}	362.7	165.7
	9 h	−0.095	3.05×10^{-6}	330.9	157.3

$1.17 \times 10^7\ \Omega\ cm^2$ for the $Ta(Si_{0.875}Al_{0.125})_2$ coating. This increasing order of R_p values is in agreement with the increased protective capability of the passive film grown on the tested samples. As shown in Table 4, for all the tested samples under cavitation erosion conditions, the resistance (R_p) values of the outer layer are negligible as compared to the resistance (R_b) of the inner layer. This is because the porous outer layer contains highly defective or microscopic pores, acting as short-circuiting paths for the penetration of species from the electrolyte. Therefore, the inner dense layer is predominantly responsible for corrosion resistance of the tested specimens under cavitation erosion conditions. Moreover, the exponent, n, of a constant phase element (CPE) reflects the heterogeneity of the passive films due to the presence of defects and is regarded as an indicator of passive film quality [46]. The lower n values usually mean that a passive film exhibits a rough and porous surface. With increasing ultrasonic cavitation time, both the resistance (R_p and R_b) and n (n_p and n_b) values decrease. These results indicate that an increase in the ultrasonic cavitation time leads not only to a significant increase the number of defects for the porous outer layer, but also defects extending towards the dense outer layer. At a given cavitation time, the resistance values for the $Ta(Si_{0.875}Al_{0.125})_2$ coating are apparently higher than those of the binary $TaSi_2$ coating and the bare Ti-6Al-4V alloy, denoting the beneficial effect of Al alloying on the cavitation corrosion performance of the $TaSi_2$ coating.

3.4.4. XPS analysis

To gain a deeper understanding of the effect of Al alloying on the composition and chemical states of the elements present in passive films formed during cavitation tests, XPS analysis was carried out on the surface of the two $Ta(Si_{1-x}Al_x)_2$ coatings after 3 h of cavitation erosion testing in a 0.5 M HCl solution under a given output power of 800 W. The XPS survey spectrum for the $Ta(Si_{0.875}Al_{0.125})_2$ coating (Fig. 15(a)) shows the Ta 4f, Si 2p, O1s and Al 2p core level principal peaks, whereas for the $TaSi_2$ coating, no Al 2p peaks were determined, as expected. A small C 1s peak appeared at 284.7 eV with negligible intensity that originated from a contaminant hydrocarbon layer covering the specimen surface. From Fig. 15(b), the measured Ta 4f photoelectron spectrum for the binary $TaSi_2$ coating was composed of one doublet peaks from $4f_{7/2}$ and $4f_{5/2}$ located at 26.3 and 28.2 eV, which corresponds to the binding energy of Ta in stoichiometric Ta_2O_5 [47]. In Fig. 15(c), the measured Si 2p spectrum for the $TaSi_2$ coating shows one component with a binding energy at about 103.6 eV, corresponding to Si in the form of fully oxidized SiO_2 [48]. In Fig. 15(d), an O 1s signal was recorded for the $TaSi_2$ coating that exhibited a broad peak, which can be fitted with two overlapped peaks: the lower binding energy peak, centered at 530.5 eV, can be assigned to O^{2-} ions, the higher binding energy peak, centered at 531.4 eV, can be attributed to adsorbed hydroxyl groups [49]. For the $Ta(Si_{0.875}Al_{0.125})_2$ coating, the Al 2p spectrum, shown in Fig. 15(e), appears as single peak centered at a binding energy of 74.4 eV, corresponding to oxidized aluminum (Al_2O_3). It is noteworthy that the Ta 4f peaks for the Ta $(Si_{0.875}Al_{0.125})_2$ coating (Fig. 15(b)) shifted towards higher binding energy as compared to the binary $TaSi_2$ coating. This is due to the interaction between Ta and Al, leading to charge transfer from Al^{3+} to Ta^{5+} ions in the passive films [50]. Fig. 15(f) shows the content of the main components present in the passive films on the two coatings. As presented in Fig. 15(f), the passive film grown on the $Ta(Si_{0.875}Al_{0.125})_2$ coating has lower Ta_2O_5 concentrations and higher SiO_2 concentrations as compared to the passive film present on the binary $TaSi_2$ coating. Compared with Ta_2O_5, SiO_2 exhibits higher dielectric characteristics together with a smaller oxygen diffusion coefficient [51]. Hence, Al additions promote SiO_2 enrichment in passive film, which is conducive to the improvement in the corrosion resistance for the $Ta(Si_{1-x}Al_x)_2$ coatings.

3.4.5. Weight loss measurements and eroded-corroded surface morphologies

Fig. 16 shows the cumulative weight loss of the two $Ta(Si_{1-x}Al_x)_2$ coatings and uncoated Ti-6Al-4V as a function of cavitation time in distilled water and in a 0.5 M HCl solution under a given output power of 800 W. For the cavitation erosion tests in distilled water, the variation of cumulative weight losses with cavitation time can be divided into two distinct stages: an incubation stage with a negligible weight loss and subsequently a slight increase stage. It is obvious that the incubation period for the uncoated alloy is shorter than the two coatings in distilled water. However, no incubation period was observed for the samples tested in a 0.5 M HCl solution, and the cumulative weight losses increase steadily with increases in cavitation time. A discrepancy in cavitation erosion properties in the two cavitating solutions can be directly traceable to the synergy between the cavitation erosion and corrosion processes that play an important role in controlling the cavitation erosion resistance of the tested samples. Whether in a 0.5 M HCl solution or in distilled water, the weight loss of the $TaSi_2$ coating is markedly decreased as compared to the uncoated counterpart. A further decrease is achieved by the $Ta(Si_{0.875}Al_{0.125})_2$ coating.

Fig. 17 presents the evolution of the eroded-corroded surface morphologies of the two $Ta(Si_{1-x}Al_x)_2$ coatings and bare Ti-6Al-4V after different cavitation exposure times in a 0.5 M HCl solution at a given output power of 800 W. As shown in Fig. 17 (b), for the uncoated alloy after 3 h of cavitation erosion, the original smooth surface becomes broken up and material removal is characterized by ductile fracture, accompanied by the roughened surface appearance containing numerous micro-craters. With increasing the cavitation time to 6 h and 9 h (Fig. 17 (c) and (d)), the uncoated alloy suffered more severe cavitation damage with some coalescence of micro-craters that developed into larger and deeper craters induced by micro-plastic deformation, yielding a honeycomb appearance. Ti-6Al-4V is a two-phase alloy composed of α-Ti and intergranular β-Ti, where there is disparity in strength between the harder α-Ti and the softer β-Ti phases [1]. Because cavitation erosion is a fatigue process, the selective erosion damage is more likely to occur at the α/β grain boundaries and this subsequently propagates into the α-Ti grains [10]. Meanwhile, the surface passive film formed on the alloy is easily disrupted by mechanical shock generated from bubble collapse. As the cavitation erosion process continues, the Ti-6Al-4V alloy sample contains a high density of defects, such as pores and cracks. Such a rough and porous surface not only increases the number of nucleation sites for bubbles, but also is detrimental to surface repassivation [52]. By comparison, as shown in Fig. 17 (f), after 3 h of the cavitation erosion test, the $TaSi_2$ coating still exhibited the as-deposited surface morphology, except a small number of shallow craters with an average diameter of ~13 μm. These craters originated from brittle delamination of the outermost layer of the $TaSi_2$ coating. With increasing cavitation time (Fig. 17 (g) and (h)), the number and size of these craters increased, although much of the as-deposited surface remained relatively smooth. For the $Ta(Si_{0.875}Al_{0.125})_2$ coating, the entire eroded surface exhibited a smooth and compact appearance with almost no visible cavitation craters, after testing for three hours (Fig. 17 (j)). With prolonging cavitation exposure time (Fig. 17 (k) and (l)), a number of small and

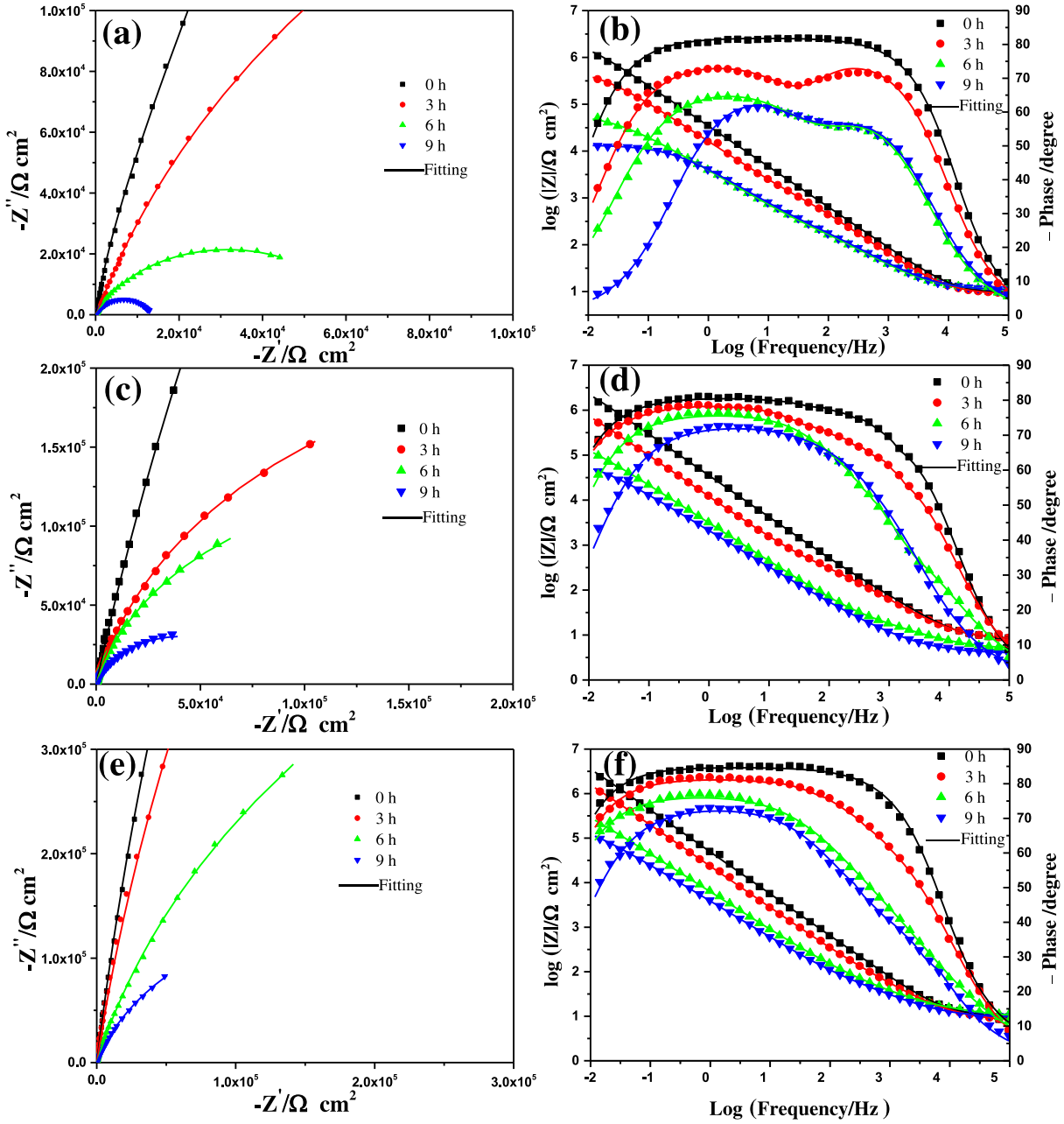

Fig. 13. Nyquist and Bode plots collected from Ti-6Al-4V and the two coatings the in a 0.5 M HCl solution after different intervals of ultrasonic cavitation erosion with the output power of 800 W. the Ti-6Al-4V ((a),(b)), $TaSi_2$ coating ((c),(d)) and $Ta(Si_{0.875}Al_{0.125})_2$ coating ((e),(f)).

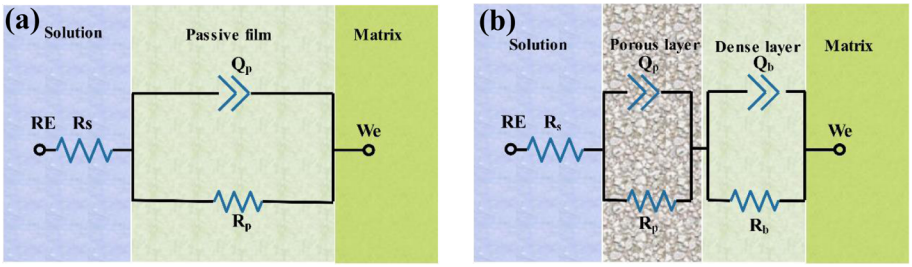

Fig. 14. Electronic equivalent circuit (EEC) used in the fitting procedure: (a) Ti-6Al-4V and $TaSi_2$ coating cavitated for 0 h, Ta $(Si_{0.875}Al_{0.125})_2$ coating cavitated for 0 h and 3 h. (b) Ti-6Al-4V and $TaSi_2$ coating cavitated for 3 h, 6 h and 9 h, Ta $(Si_{0.875}Al_{0.125})_2$ coating cavitated for 6 h and 9 h.

shallow craters appeared. These had an average diameter of ~7 μm after 6 h of exposure time and 9 μm after 9 h of exposure time. However, most of the coating surface exhibited little surface damage. It is evident that Al alloying acts to improve the cavitation erosion resistance of the $TaSi_2$ coating, since the eroded surface of the $Ta(Si_{0.875}Al_{0.125})_2$ coating exhibited fewer and smaller craters than that of the $TaSi_2$ coating.

Table 4
Electrochemical parameters obtained from numerical fitting for the uncoated Ti-6Al-4V and two coatings after cavitated for different time at an output power of 800 W.

Ti-6Al-4V	0 h	$R_s(Q_bR_b)$							
		R_s (Ω cm^2)	Q_p (Ω^{-1}cm^{-2}s^n)	n_p	R_p (Ω cm^2)				χ^2
		10.43	3.22×10^{-6}	0.90	4.62×10^6				2.43×10^{-3}
		$R_s(Q_pR_p)(Q_bR_b)$							
		R_s (Ω cm^2)	Q_p (Ω^{-1} cm^{-2} s^n)	n_p	R_p (Ω cm^2)	Q_b (Ω^{-1} cm^{-2}s^n)	n_b	R_b (Ω cm^2)	χ^2
	3 h	8.81	1.815×10^{-5}	0.79	100.82	1.33×10^{-5}	0.83	5.41×10^5	2.65×10^{-3}
	6 h	10.86	8.80×10^{-5}	0.77	80.53	6.21×10^{-5}	0.78	6.31×10^4	1.02×10^{-3}
	9 h	10.57	1.02×10^{-4}	0.72	71.18	9.15×10^{-5}	0.76	1.33×10^4	8.25×10^{-4}
$TaSi_2$	0 h	$R_s(Q_bR_b)$							
		R_s (Ω cm^2)	Q_p (Ω^{-1}cm^{-2}s^n)	n_p	R_p (Ω cm^2)				χ^2
		8.54	7.62×10^{-6}	0.91	8.52×10^6				2.56×10^{-3}
		$R_s(Q_pR_p)(Q_bR_b)$							
		R_s (Ω cm^2)	Q_p (Ω^{-1} cm^{-2} s^n)	n_{op}	R_p (Ω cm^2)	Q_b (Ω^{-1} cm^{-2}s^n)	n_b	R_b (Ω cm^2)	χ^2
	3 h	6.19	1.27×10^{-5}	0.84	140.93	9.67×10^{-6}	0.86	5.73×10^5	1.65×10^{-3}
	6 h	4.71	2.66×10^{-5}	0.82	123.61	4.77×10^{-5}	0.84	3.19×10^5	7.24×10^{-4}
	9 h	3.83	9.76×10^{-5}	0.79	89.27	8.02×10^{-5}	0.81	8.13×10^4	1.23×10^{-3}
$Ta(Si_{0.875}Al_{0.125})_2$	0 h	$R_s(Q_bR_b)$							
		R_s (Ω cm^2)	Q_p (Ω^{-1}cm^{-2}s^n)	n_p	R_p (Ω cm^2)				χ^2
		8.01	4.66×10^{-6}	0.93	1.17×10^7				1.78×10^{-3}
	3 h	9.65	9.07×10^{-6}	0.89	6.51×10^6				1.63×10^{-3}
		$R_s(Q_pR_p)(Q_bR_b)$							
		R_s (Ω cm^2)	Q_p (Ω^{-1} cm^{-2} s^n)	n_p	R_p (Ω cm^2)	Q_b (Ω^{-1} cm^{-2}s^n)	n_b	R_b (Ω cm^2)	χ^2
	6 h	11.12	1.79×10^{-5}	0.82	129.76	2.65×10^{-5}	0.85	1.37×10^6	7.97×10^{-4}
	9 h	9.78	7.49×10^{-5}	0.80	100.68	2.29×10^{-5}	0.82	5.36×10^5	8.65×10^{-4}

4. Discussion

Cavitation erosion resistance of a material is affected by several factors, which depend, not only upon mechanical properties, including hardness, fracture energy, tensile strength, Young's modulus, fatigue strength, but also on the cavitation experimental conditions, such as the aggressiveness, flow velocity and temperature of cavitating liquid, gas content and the intensity of cavitation [53]. Understanding the key parameter responsible for the cavitation erosion resistance of a specific material is essential in explaining its degradation mechanism. Kaspar et al. [54] studied the cavitation erosion resistance of laser nitrided Ti-6Al-4V under different gas atmospheres in deionized water. Their results showed an inversely proportional relationship between cavitation erosion rate and the hardness of laser nitride layer is tenable under gas atmospheres with N contents between 0 and 13%. However, the erosion rate did not reduce further with greater increases in surface hardness. In our case, the reverse tendency seems to occur, i.e. the cavitation erosion rate of the $Ta(Si_{1-x}Al_x)_2$ coatings was proportional to the coating hardness. H/E and H^3/E^2 ratios have been previously used as suitable indicators to predict the tribological performance of materials. Recently, several studies have also attempted to correlate cavitation erosion resistance to these ratios [55,56]. However, apparent contradictions involving the relationship among those ratios and erosion rates have been observed [57,58]. Our experimental results also indicate that these ratios bear no clear relation to cavitation erosion resistance of the two $Ta(Si_{1-x}Al_x)_2$ coatings. The H/E and H^3/E^2 ratios for the $TaSi_2$ and the $Ta(Si_{0.875}Al_{0.125})_2$ coatings are approximately equal, as presented in Fig. 8(e). However, from the eroded-corroded surface morphologies of the two $Ta(Si_{1-x}Al_x)_2$ coatings (Fig. 17), cavitation craters appeared to result from the fracture and delamination of the coatings. This suggests the surface degradation of these coatings occurred in a brittle manner. Therefore, it appears that fracture toughness is the most relevant mechanical property which governs the cavitation erosion resistance of these $Ta(Si_{1-x}Al_x)_2$ coatings. According to the results obtained from first-principle calculations, Al additions can improve the toughness of $TaSi_2$, which is consistent with the observations from cavitation erosion testing. Moreover, in the case of the hard $Ta(Si_{1-x}Al_x)_2$ coating-soft Ti-6Al-4V substrate system, there is remarkable difference in mechanical properties between the coatings and Ti-6Al-4V substrate. For example, the two $Ta(Si_{1-x}Al_x)_2$ coatings have approximately three times greater Young's modulus than the Ti-6Al-4V substrate. During the cavitation erosion process, the $Ta(Si_{1-x}Al_x)_2$ coating and Ti-6Al-4V substrate show different responses to impact loading exerted by the cavitation pulses. During the unloading process, the $Ta(Si_{1-x}Al_x)_2$ coatings exhibit a higher relaxation rate than the Ti-6Al-4V substrate, but the coating/substrate adhesion requires the coating to adjust to the deformed Ti-6Al-4V substrate to ensure they relax together. This leads to increased residual stresses in the coating and the decreased adhesion of the coating to the substrate [59]. Compared with the binary $TaSi_2$ coating, the ternary $Ta(Si_{0.875}Al_{0.125})_2$ coating possesses a higher adhesion strength, which is beneficial in reducing coating delamination during cavitation erosion process. Alternatively, when the tested samples are exposed to a corrosive cavitating liquid, the surface passive film and its repair capacity play a crucial role in their cavitation erosion resistance, due to the presence of the synergetic effect between mechanical erosion and electrochemical corrosion. The mechanical action of bubble implosion can accelerate removal of an existing passive film or reduce its thickness, thereby exposing the underlying fresh surface. This phenomenon is further supported by the obvious rise in current density under the hydrodynamic conditions that is registered with respect to the static conditions. Subsequently, the galvanic coupling between the mechanically depassivated areas and the surrounding passive areas is created, resulting in an increment of I_{corr} value and an active shift of E_{corr} as shown in Fig. 12. The damaged passive film can be subsequently reformed due to re-passivation and the erosion rate of the tested samples depends on the competition between the thinning or removal of passive films and its self-healing capability [60]. According to the above electrochemical measurements, Al additions enhance the thermodynamic stability and the self-healing capability of the passive film on the $TaSi_2$ coating, thus improving its cavitation erosion resistance.

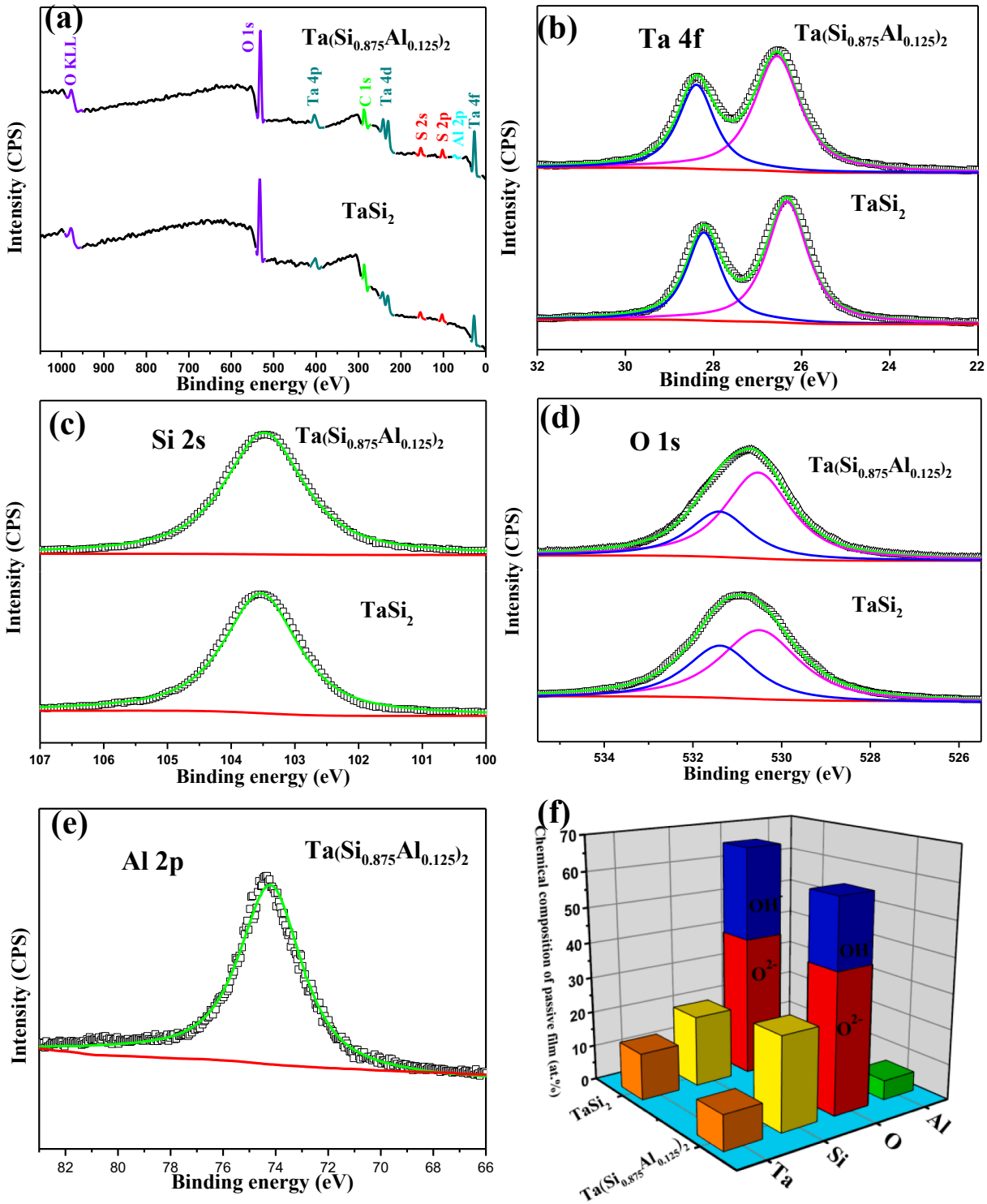

Fig. 15. XPS survey spectrum spectra (a) and the high-resolution XPS spectra for (b) Ta, (c) Si, (d) O and (e) Al for the $TaSi_2$ coating and $Ta(Si_{0.875}Al_{0.125})_2$ coating after 3 h of cavitation erosion testing in a 0.5 M HCl solution under a given output power of 800 W; (f) the content of the main components present in the passive films on the two coatings.

5. Conclusions

The influence of Al alloying on the structural stability and mechanical behavior of C40-structured $TaSi_2$ was investigated by first-principles methods. In the light of these theoretical calculations, a $Ta(Si_{0.875}Al_{0.125})_2$ compound was selected as an appropriate Al addition to prepare an Al-alloyed $TaSi_2$ coating using a double cathode glow discharge plasma method. Following detailed microstructural characterization and mechanical property measurements, the electrochemical behavior of the binary $TaSi_2$ and ternary $Ta(Si_{0.875}Al_{0.125})_2$ coatings in a 0.5 M HCl

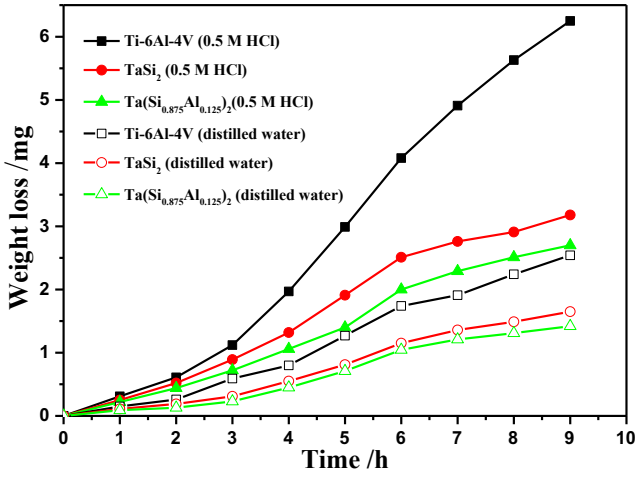

Fig. 16. The weight loss as a function of time for Ti-6Al-4V and two coating specimens at an output power of 800 W in distilled water and a 0.5 M HCl solution, respectively.

solution was determined by means of various electrochemical analytical techniques under ultrasonic cavitation erosion conditions. The following conclusions can be drawn:

(1) Theoretical studies on the mechanical properties of $Ta(Si_{1-x}Al_x)_2$ compounds show that a significant increase in plasticity as Al content increases from 0 to 12.5 at.%, but with a negligible change in plasticity after further additions of Al.
(2) The $Ta(Si_{1-x}Al_x)_2$ coatings exhibit a uniform thickness and dense structure, composed of spherically shaped nanocrystallites with an average diameter of about 5 nm. The hardness values of the $TaSi_2$ and $Ta(Si_{0.875}Al_{0.125})_2$ coatings are about 4.4 and 4.1 times greater, respectively, than that of uncoated Ti-6Al-4V substrate. The Al addition increases the ratio of W_p/W_t of the $Ta(Si_{1-x}Al_x)_2$ coating, suggesting that Al alloying enhances the plastic deformation capability of the $TaSi_2$ coating.
(3) The results of electrochemical measurements indicate that the Al addition enhances the thermodynamic stability and the self-healing capability of the passive film on the $Ta(Si_{1-x}Al_x)_2$ coating, thus improving its cavitation erosion resistance.

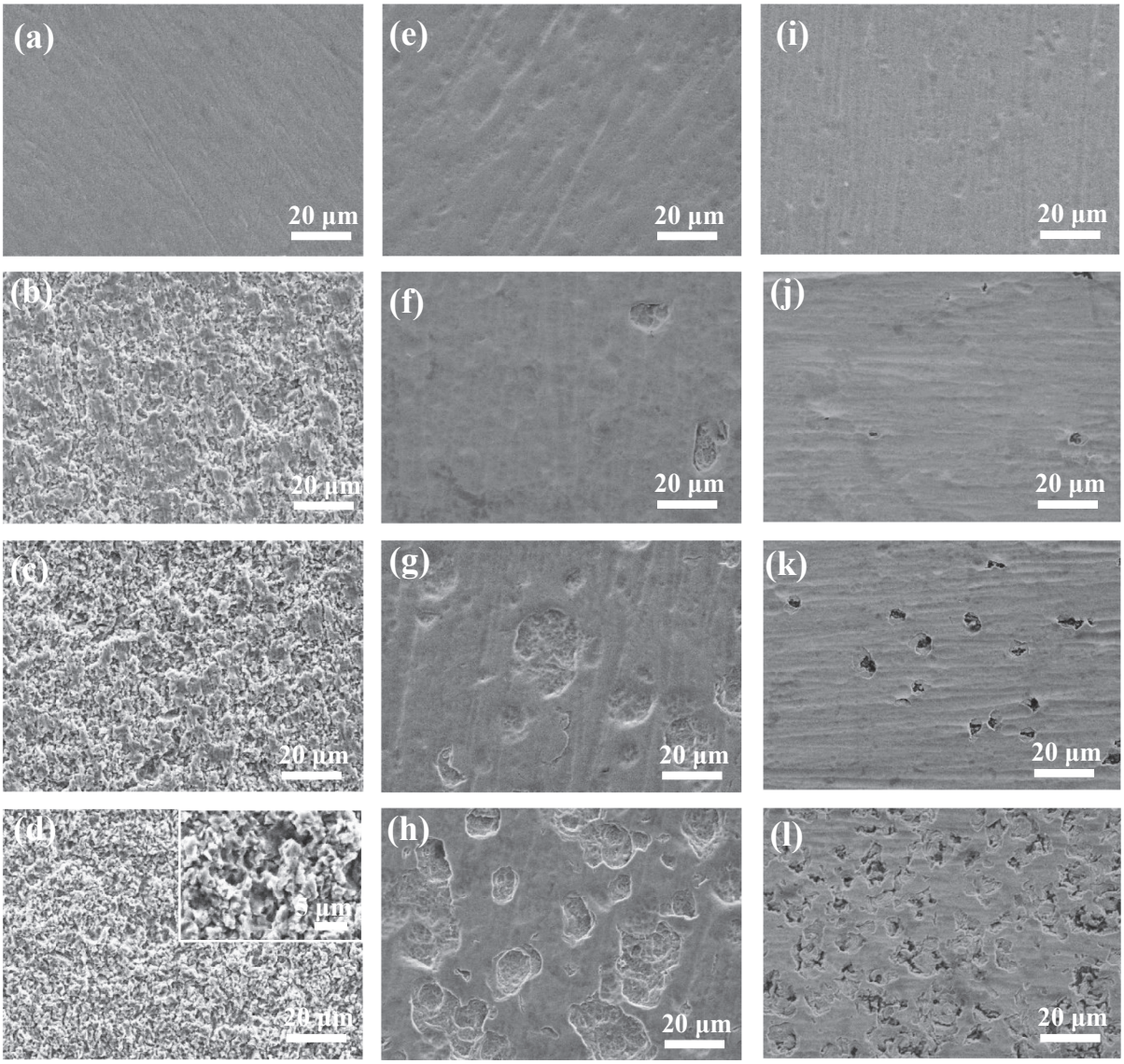

Fig. 17. Surface morphologies of damaged surfaces for Ti-6Al-4V (a) 0 h, (b) 3 h, (c) 6 h, (d) 9 h; $TaSi_2$ coating (e) 0 h, (f) 3 h, (g) 6 h, (h) 9 h; $Ta(Si_{0.875}Al_{0.125})_2$ coating (i) 0 h, (j) 3 h, (k) 6 h, (l) after cavitation erosion under output power of 800 W in a 0.5 mol/l HCl solution.

Acknowledgements

The authors acknowledge the financial support of the General Program of the National Natural Science Foundation of China under Grant No. 51675267, the Key Program of the National Natural Science Foundation of China under Grant No. 51635004.

References

[1] H.B. Li, Z.D. Cui, Z.Y. Li, S.L. Zhu, X.J. Yang, Effect of gas nitriding treatment on cavitation erosion behavior of commercially pure Ti and Ti-6Al-4V alloy, Surf. Coat. Technol. 221 (2013) 29–36.
[2] D.G. Li, J.D. Wang, D.R. Chen, P. Liang, Ultrasonic cavitation erosion of Ti in 0.35% NaCl solution with bubbling oxygen and nitrogen, Ultrason. Sonochem 26 (2015) 99–110.
[3] J. Stella, E. Schuller, C. Heβing, O.A. Hamed, M. Pohl, D. Stover, Cavitation erosion of plasma-sprayed NiTi coatings, Wear 260 (2006) 1020–1027.
[4] K.Y. Chiu, F.T. Cheng, H.C. Man, Laser cladding of austenitic stainless steel using NiTi strips for resisting cavitation erosion, Mater. Sci. Eng. A 402 (2005) 126–134.
[5] K. Selvam, P. Mandal, H.S. Grewal, H.S. Arora, Ultrasonic cavitation erosion-corrosion behavior of friction stir processed stainless steel, Ultrason. Sonochem. 44 (2018) 331–339.
[6] G.L. Hou, X.Q. Zhao, H.D. Zhou, J.J. Lu, Y.L. An, J.M. Chen, J. Yang, Cavitation erosion of several oxy-fuel sprayed coatings tested in deionized water and artificial seawater, Wear 311 (2014) 81–92.
[7] H. Mochizuki, M. Yokota, S.J. Hattori, Effects of materials and solution temperatures on cavitation erosion of pure titanium and titanium alloy in seawater, Wear 262 (2007) 522–528.
[8] D.G. Li, Y. Long, P. Liang, D.R. Chen, Effect of micro-particles on cavitation erosion of Ti6Al4V alloy in sulfuric acid solution, Ultrason. Sonochem. 36 (2017) 270–276.
[9] B.S. Mann, Vivek Arya, B.K. Pant, Cavitation erosion behavior of HPDL-treated TWAS-coated Ti6Al4V alloy and its similarity with water droplet erosion, J. Mater. Eng. Perform. 21 (2012) 849–853.
[10] H.C. Man, Z.D. Cui, T.M. Yue, F.T. Cheng, Cavitation erosion behavior of laser gas nitrided Ti and Ti6Al4V alloy, Mater. Sci. Eng. A 355 (2003) 167–173.
[11] J. Xu, D.H. Lai, Z.H. Xie, P. Munroe, Z.T. Jiang, A critical role for Al in regulating the corrosion resistance of nanocrystalline $Mo(Si_{1-x}Al_x)_2$ films, J. Mater. Chem. 29 (16) (2011) 3083–3088.
[12] Y. Niu, L.P. Huang, C.H. Zhai, Y. Zeng, X.B. Zheng, C.X. Ding, Microstructure and thermal stability of $TaSi_2$ coating fabricated by vacuum plasma spray, Surf. Coat. Technol. 279 (2015) 1–8.
[13] J. Xu, W. Liu, Shuyun Jiang, P. Munroe, Z.H. Xie, Enhancing the cavitation erosion resistance of D8m-Ta_5Si_3 nanocrystalline coatings through Al alloying, Ultrason. Sonochem. 50 (2019) 138–156.
[14] H. Hu, X.Z. Wu, R. Wang, W.G. Li, Q. Liu, First principles study on the phase stability and mechanical properties of $MoSi_2$ alloyed with Al, Mg and Ge, Intermetallics 67 (2015) 26–34.
[15] M.D. Segall, P.J.D. Lindan, M.J. Probert, C.J. Pickard, P.J. Hasnip, S.J. Clark, M.C. Payne, First-principles simulation: ideas, illustrations and the CASTEP code, J. Phys.: Condens. Matter 14 (2002) 2717–2744.
[16] J.P. Perdew, Y. Wang, Accurate and simple analytic representation of the electron-gas correlation energy, Phys. Rev. B 45 (23) (1992) 13244–13249.
[17] V. Kumar, B.P. Singh, B.P. Pandey, First-principle calculations of the elastic properties of AIIBIVCV 2C2V semiconductors, Comput. Mater. Sci. 87 (2014) 227–231.
[18] R.D. Zhao, F.F. Wu, X. Liu, J.C. Zhu, Z.F. Zhao, First-principles study of Mn alloying into Fe_3AlC: towards the improvement of ductility, J. Alloy. Compd. 681 (2016) 283–292.
[19] W.C. Oliver, G.M. Pharr, An improved technique for determining hardness and elastic modulus using load and displacement sensing indentation experiments, J. Mater. Res. 7 (6) (1992) 1564–1583.
[20] ASTM Standard Test Method for Cavitation Erosion Using Vibratory Apparatus, Standard G32-16, 2016.
[21] B. Wan, F. Xiao, Y.K. Zhang, Y. Zhao, L.L. Wu, J.W. Zhang, H.Y. Gou, Theoretical study of structural characteristics, mechanical properties and electronic structure of metal (TM = V, Nb and Ta) silicides, J. Alloy. Compd. 681 (2016) 412–420.
[22] Y. Pan, Y.H. Lin, Q. Xue, C.Q. Ren, H. Wang, Relationship between Si concentration and mechanical properties of Nb-Si compounds: a first-principles study, Mater. Des. 89 (2016) 676–683.
[23] Y.F. Li, Y.M. Gao, B. Xiao, T. Min, Z.J. Fan, S.Q. Ma, L.L. Xu, Theoretical study on the stability, elasticity, hardness and electronic structures of W-C binary compounds, J. Alloy. Compd. 502 (2010) 28–37.
[24] F. Chu, M. Lei, S.A. Maloy, J.J. Petrovic, T.E. Mitchell, Elastic properties of C40 transition metal disilicides, Acta Mater. 44 (8) (1996) 3035–3048.
[25] Y. Pan, J. Zhang, C. Jin, X.Y. Chen, Influence of vacancy on structural and elastic properties of $NbSi_2$ from first-principles calculations, Mater. Des. 108 (2016) 13–18.
[26] Y. Pan, W.M. Guan, Effect of sulfur concentration on structural, elastic and electronic properties of molybdenum sulfides from first-principles, Int. J. Hydrogen. Energy 41 (2016) 11033–11041.
[27] X.Q. Chen, H.Y. Niu, D.Z. Li, Y.Y. Li, Modeling hardness of polycrystalline materials and bulk metallic glasses, Intermetallics 19 (2011) 1275–1281.
[28] H. Wang, H.Z. Zeng, Q.K. Li, J. Shen, Superlattice supertoughness of TiN/MN (M = V, Nb, Ta, Mo, and W): first-principles study, Thin Solid Films 607 (2016) 59–66.
[29] I.J. Shon, I.Y. Ko, S.M. Chae, K.I. Na, Rapid consolidation of nanostructured $TaSi_2$ from mechanochemically synthesized powder by high frequency induction heated sintering, Ceram. Int. 37 (2011) 679–682.
[30] C.J. Cui, J. Zhang, L. Liu, H.Z. Fu, Mechanical properties of the $TaSi_2$ fibers by nanoindentation, J. Mater. Sci. Technol. 26 (1) (2016) 65–68.
[31] J. Xu, J. Cheng, S.Y. Jiang, P. Munroe, Z.H. Xie, The influence of Ti additions on the mechanical and electrochemical behavior of β-Ta_5Si_3 nanocrystalline coating, Appl. Surf. Sci. 419 (2017) 901–915.
[32] R. Liu, D.Y. Li, Y.S. Xie, R. Liewellyn, H.M. Hawthorne, Indentation behavior of pseudoelastic TiNi alloy, Scr. Mater. 41 (7) (1999) 691–696.
[33] R.K. Wade, J.J. Petrovic, Fracture modes in $MoSi_2$, J. Am. Ceram. Soc. 75 (1992) 1682–1684.
[34] P. Peralta, R. Dickerson, J.R. Michael, K.J. McClellan, F. Chu, T.E. Mitchell, Residual thermal stresses in $MoSi_2$-Mo_5Si_3 in-situ composites, Mater. Sci. Eng. A 261 (1999) 261–269.
[35] H. Bei, E.P. Georgea, G.M. Pharr, Effects of composition on lamellar microstructures of near-eutectic Cr-Cr_3Si alloys, Intermetallics 11 (2003) 283–289.
[36] D.G. Morris, M. Leboeuf, M.A. Morris, Hardness and toughness of $MoSi_2$ and $MoSi_2$-SiC composite prepared by reactive sintering of powders, Mater. Sci. Eng. A 251 (1998) 262–268.
[37] K.W. Chen, J.F. Lin, Investigation of the relationship between primary and secondary shear bands induced by indentation in bulk metallic glasses, Int. J. Plast. 26 (2010) 1645–1658.
[38] J.J. Kim, Y. Choi, S. Suresh, A.S. Argon, Nanocrystallization during nanoindentation of a bulk amorphous metal alloy at room temperature, Science 295 (5555) (2002) 654–657.
[39] P.C. Wo, P.R. Munroe, Z.F. Zhou, K.Y. Li, Z.H. Xie, Effects of TiN sublayers on the response of TiSiN nanocomposite coatings to nanoidentation and scratching contacts, Mater. Sci. Eng. A 527 (2010) 4447–4457.
[40] L.W. Ma, J.M. Cairney, M.J. Hoffman, P.R. Munroe, Deformation and fracture of TiN and TiAlN coatings on a steel substrate during nanoindentation, Surf. Coat. Technol. 200 (2006) 3518–3526.
[41] L.W. Ma, J.M. Cairney, M.J. Hoffman, P.R. Munroe, Effect of coating thickness on the deformation mechanisms in PVD TiN-coated steel, Surf. Coat. Technol. 204 (11) (2010) 1764–1773.
[42] C.T. Kwok, H.C. Man, F.T. Cheng, Cavitation erosion-corrosion behaviour of laser surface alloyed AISI 1050 mild steel using NiCrSiB, Mater. Sci. Eng. A 303 (2001) 250–261.
[43] H. Ashassi-Sorkhabi, N. Ghalebsaz-Jeddi, Effect of ultrasonically induced cavitation on inhibition behavior of polyethylene glycol on carbon steel corrosion, Ultrason. Sonochem. 13 (2006) 180–188.
[44] R.M. Fernandez-Domene, E. Blasco-Tamarit, D.M. Garcia-Garcia, J. Garcia-Anton, Repassivation of the damage generated by cavitation on UNS N08031 in a LiBr solution by means of electrochemical techniques and confocal laser scanning microscopy, Corros. Sci. 52 (2010) 3453–3464.
[45] D.G. Li, J.D. Wang, D.R. Chen, P. Liang, The role of passive potential in ultrasonic cavitation erosion of titanium in 1 M HCl solution, Ultrason. Sonochem. 29 (2016) 279–287.
[46] B. Munirathinam, R. Narayanan, L. Neelakantan, Electrochemical and semiconducting properties of thin passive film formed on titanium in chloride medium at various pH conditions, Thin Solid Films 598 (2016) 260–270.
[47] B.C. Wang, J.H. Zhu, Influence of ultrasonic cavitation on passive film of stainless steel, Ultrason. Sonochem. 15 (2008) 239–243.
[48] M.H. Li, G. Han, Y. Liu, C. Feng, H.C. Wang, J. Teng, G.H. Yu, XPS analyses of Ta/MgO_x/$Ni_{81}Fe_{19}$/MgO_x/Ta films, Appl. Surf. Sci. 258 (2012) 9589–9592.
[49] A.M.G. Tavares, B.S. Fernandes, S.A. Souza, W.W. Batista, F.G.C. Cunha, R. Landers, M.C.S.S. Macedo, The addition of Si to the Ti-35Nb alloy and its effect on the corrosion resistance, when applied to biomedical materials, J. Alloy. Compd. 591 (2014) 91–99.
[50] C. Vasilescu, S.I. Drob, J.M. Calderon Moreno, P. Osiceanu, M. Popa, E. Vasilescu, M. Marcu, P. Drob, Long-term corrosion resistance of new Ti-Ta-Zr alloy in simulated physiological fluids by electrochemical and surface analysis methods, Corros. Sci. 93 (2015) 310–323.
[51] M. Zier, S. Oswald, R. Reiche, M. Kozlowska, K. Wetzig, Interface formation and reactions at Ta-Si and Ta-SiO_2 interfaces studied by XPS and ARXPS, J. Electron. Spectrosc. Relat. Phenom. 137–140 (2004) 229–233.
[52] Z.L. Jiang, X. Dai, H. Middleton, Effect of silicon on corrosion resistance of Ti-Si alloys, Mater. Sci. Eng. B 176 (2011) 79–86.
[53] C.L. Wu, S. Zhang, C.H. Zhang, H. Zhang, S.Y. Dong, Phase evolution and cavitation erosion-corrosion behavior of FeCoCrAlNiTi_x high entropy alloy coatings on 304 stainless steel by laser surface alloying, J. Alloy. Compd. 698 (2017) 761–770.
[54] A.K. Krella, The new parameter to assess cavitation erosion resistance of hard PVD coatings, Eng. Fail. Anal. 18 (2011) 855–867.
[55] J. Kaspar, J. Bretschneider, S. Jacob, S. Bonβ, B. Winderlich, B. Brenner, Microstructure, hardness and cavitation erosion behaviour of Ti-6Al-4V laser nitrided under different gas atmospheres, Surf. Eng. 23 (2) (2007) 99–106.
[56] P.C. Wang, Y.T. Shih, M.C. Lin, H.C. Lin, M.J. Chen, K.M. Lin, Improvement of wear and cavitation–erosion by ALD-deposited $LiAl_xO_y$ films on an Mg-10Li-0.5Zn alloy, Surf. Coat. Technol. 204 (2010) 3707–3712.

[57] L.A. Espitia, H.S. Dong, X.Y. Li, C.E. Pinedo, A.P. Tschiptschin, Cavitation erosion resistance and wear mechanisms of active screen low temperature plasma nitride AISI 410 martensitic stainless steel, Wear 332–333 (2015) 1070–1079.
[58] M.M. Lima, C. Godoy, P.J. Modenesi, J.C. Avelar-Batista, A. Davison, A. Matthews, Coating fracture toughness determined by Vickers indentation: an important parameter in cavitation erosion resistance of WC-Co thermally sprayed coatings, Surf. Coat. Technol. 177–178 (2004) 489–496.
[59] C.K. Lin, C.H. Hsu, Y.H. Cheng, A study on the corrosion and erosion behavior of electroless nickeland TiAlN/ZrN duplex coatings on ductile iron, Appl. Surf. Sci. 324 (2015) 13–19.
[60] A.K. Krella, The experimental resistance parameter for TiN coating to cavitation action, Adv. Mater. Sci. 10 (1) (2010) 4–18.